Laminar Boundary Layer Development Around a Circular Cylinder: Fluid Flow and Heat-Mass Transfer Characteristics

A. Alper Ozalp[1]
Department of Mechanical Engineering,
University of Uludag,
16059 Gorukle, Bursa, Turkey
e-mail: aozalp@uludag.edu.tr

Ibrahim Dincer
Faculty of Engineering and Applied Science,
University of Ontario Institute of Technology,
2000 Simcoe Street North,
Oshawa, ON L1H 7K4, Canada
e-mail: ibrahim.dincer@uoit.ca

This paper presents a comprehensive computational work on the hydrodynamic, thermal, and mass transfer characteristics of a circular cylinder, subjected to confined flow at the cylinder Reynolds number of $Re_d=40$. As the two-dimensional, steady and incompressible momentum and energy equations are solved using ANSYS-CFX (version 11.0), the moisture distributions are computed by a new alternating direction implicit method based software. The significant results, highlighting the influence of blockage ($\beta=0.200-0.800$) on the flow and heat transfer mechanism and clarifying the combined roles of β and moisture diffusivity ($D=1\times10^{-8}-1\times10^{-5}$ m^2/s) on the mass transfer behavior, are obtained for practical applications. It is shown that the blockage augments the friction coefficients (C_f) and Nusselt numbers (Nu) on the complete cylinder surface, where the average Nu are evaluated as $Nu_{ave}=3.66$, 4.05, 4.97, and 6.51 for $\beta=0.200$, 0.333, 0.571, and 0.800. Moreover, the blockage shifts separation (θ_s) and maximum C_f locations (θ_{C_f-max}) downstream to the positions of $\theta_s=54.10$, 50.20, 41.98, and 37.30 deg and $\theta_{C_f-max}=51.5$, 53.4, 74.9, and 85.4 deg. The highest blockage of $\beta=0.800$ encourages the downstream backward velocity values, which as a consequence disturbs the boundary layer and weakens the fluid-solid contact. The center and average moisture contents differ significantly at the beginning of drying process, but in the last 5% of the drying period they vary only by 1.6%. Additionally, higher blockage augments mass transfer coefficients (h_m) on the overall cylinder surface; however, the growing rate of back face mass transfer coefficients (h_{m-bf}) is dominant to that of the front face values (h_{m-ff}), with the interpreting ratios of $\bar{h}_{m-bf}/\bar{h}_m=0.50$ and 0.57 and $\bar{h}_{m-ff}/\bar{h}_m=1.50$ and 1.43 for $\beta=0.200$ and 0.800. [DOI: 10.1115/1.4002288]

Keywords: heat transfer, fluid flow, mass transfer, confined flow, friction coefficient , moisture diffusivity, moisture transfer coefficient, drying

1 Introduction

Heat and mass transfer aspects of a circular cylinder (CC), subjected to fluid flow, are of considerable interest in many industrial applications, such as unit operations [1], manufacturing [2], and drying [3] processes. From the point of flow around CCs, practical applications such as flow metering devices, support structures, off-shore pipelines, and instrumentation, where small cylindrical wire probes or sensors are made to obstruct the free flow of a fluid and tall buildings, are involved in this industrial frame. As heat transfer mechanisms of CCs are closely interrelated with the operation performance of cooling towers, chimneys, heat exchangers, and cooling of electronic components and equipments, mass transfer behaviors create the technologic base not only for expert systems on food and wood drying but also for nuclear, biological, and chemical filters. For the complete application range, industrial and scientific research on mass transfer operations seeks a proper estimation of the drying time, as well as the behavior of all corresponding operational factors playing an important role in the design and optimization of the related processes. Since mass transfer mechanism depends considerably on the boundary layer development around the dissipating body and on the corresponding heat transfer behavior, the necessity in the idealization of the associated engineering designs becomes apparent. Besides, if the flow around the CC is confined, causing a blockage, both the flow and heat transfer behaviors are structured in accord with this domain dependence, which in return definitely characterizes the mass transfer characteristics. Depending on these facts, research focuses mainly on three key topics: (i) fluid flow and boundary layer development around the CC, (ii) heat transfer from the CC, and (iii) mass transfer within and from the CC.

With the onset of boundary layer investigations, fluid flow around CCs has been the subject of several recent studies. However, due to the needs of certain specific industrial applications, some recent work concentrated on the confined flow, or flow with blockage, around CCs [4–8] and even for square cylinders (SCs) [9,10]. Griffith et al. [4] numerically studied the two-dimensional flow around a CC, where their technical concerns were wake behavior, vortex shedding, recirculation, and separation lengths for the blockage range of $\beta=0.05-0.9$. In a similar computational study, Chakraborty et al. [5] worked on the blockage limits of $\beta=0.05-0.65$; where they additionally studied frictional and total drag coefficients on the CC. For the Reynolds number and blockage ratio ranges of $Re_d=0-280$ and $\beta=0.1-0.9$, numerical com-

[1]Corresponding author.

Contributed by the Heat Transfer Division of ASME for publication in the JOURNAL OF HEAT TRANSFER. Manuscript received April 4, 2010; final manuscript received July 20, 2010; published online September 20, 2010. Assoc. Editor: Ali Ebadian.

putations were performed by Sahin and Owens [6] who reported the neutral stability limit as $Re_d \approx 100$ for $\beta = 0.333-0.800$. In a similar work, Rehimi et al. [7] carried out steady and unsteady regime investigations for the particular blockage case of $\beta = 0.333$ within the Reynolds number range of $Re_d = 30-277$. They stated that for $Re_d < 108$, the streamlines and the pathlines exhibit the characteristics of a steady regime and the flow is characterized by two fixed counter-rotating vortices downstream of the cylinder. Steady numerical computations, in the Reynolds number and blockage ratio ranges of $Re_d = 6-40$ and $\beta = 0-0.8$, were performed by Sen et al. [8], where their findings covered the variation of bubble length, separation angle, and drag force characteristics. Bruer et al. [9] and Camarri and Giannetti [10] studied the identical flow scenarios for SCs for the blockage ratios of $\beta = 0.125$ [9] and $\beta = 0.1-0.17$ [10]. As steady and unsteady flow discussions on recirculation lengths and drag coefficients were presented in Ref. [9], the impact of blockage in unsteady flows, the wake interaction between the wake and the flow close to the confining walls, were clarified in Ref. [10].

There is a limited number of numerical and experimental studies on how local or mean heat transfer aspects of CCs vary with Reynolds and/or Prandtl numbers or with fluid properties. Chang and Mills [11] experimentally studied the effect of aspect ratio on the heat transfer behavior of a cylinder in cross-flow of air. They determined that the circumferentially averaged and total averaged Nusselt numbers increased with decreasing aspect ratio. The integral approach of the boundary layer analysis, to study the fluid flow and heat transfer mechanism around an infinite CC, was applied by Khan et al. [12]. They developed closed form drag and average heat transfer coefficient expressions applicable in wide ranges of Reynolds and Prandtl numbers. In one of their more recent work [13], they investigated the influence of a thin hydrodynamic boundary layer on the heat transfer from a single circular cylinder in liquid metals for a low Prandtl number (between 0.004 and 0.03) under isothermal and isoflux boundary conditions. Bharti et al. [14] numerically studied the effects of Re and Pr on average and local Nu distributions during forced convection heat transfer to incompressible Newtonian and non-Newtonian fluids from a heated circular cylinder in the steady cross-flow regime. Besides the purely CC based fluid flow and heat transfer efforts, there exist a few research that involved different types of cylinder cross sections. An experimental study, to evaluate the convective heat transfer coefficient of liquid cooled various-shaped short pin fins, by means of the infrared thermography was performed by Montelpare and Ricci [15]. Their results demonstrated that the trend of the Nusselt number at different Reynolds numbers depended heavily on the pin shape. In a more comprehensive work, Sparrow et al. [16] collected the average Nusselt number information for circular and noncircular cylinders in cross-flow of air, where some of the noncircular cross sections include squares, diamonds, flat plates perpendicular to the freestream, ellipses, and rectangles.

Considerably limited work dealt with the influence of confining walls on the heat transfer phenomena around cylinders. Buyruk et al. [17] numerically investigated the laminar flow and heat transfer characteristics of a CC for the blockage ratio range of $\beta = 0.17-0.48$. They predicted not only the local static pressure and Nusselt number variations on the CC surface but also the isotherm and streamline contours of the wake region. Through an integral approach of the boundary layer analysis, Khan et al. [18] investigated fluid flow around and heat transfer from a CC between parallel planes for $\beta = 0-0.80$. They found that the blockage ratio controls the fluid flow and the transfer of heat from the cylinder and delays the separation. The blockage effects on the laminar heat transfer mechanism of SCs were also taken into account. As Sharma and Eswaran [19] concentrated on the blockage cases of $\beta = 0.1-0.5$, Dhiman et al. [20] detailed the impact of $\beta = 0.125-0.25$ range. To produce a base for heat transfer discussions, either of the studies presented fluid flow results in terms of velocity profiles, friction and drag coefficient values, and supplied information on the wake structure for different β cases. The growth of drag coefficients and heat transfer rates with blockage were the common outcomes [19,20].

There have been considerable efforts to experimentally/computationally characterize the drying mechanism and mass transfer behavior of moist objects. As some of the work aimed to propose applicable theory for wide range of applications, others focused on specific material. Theoretical and experimental results, on the drying kinetics of bananas, under different air drying conditions, were reported by Queiroz and Nebra [21]. They investigated the effects of surface convective mass transfer by treating the experimental data of moisture content during drying through a diffusion model, where the diffusion coefficient was considered as constant. Dincer et al. [22] developed and verified new drying correlations to determine the moisture transfer parameters, such as moisture diffusivity and moisture transfer coefficients. Akpinar and Dincer [3,23] carried out the experimental and theoretical investigations on the drying of slab cut eggplant slices [3] and potato pieces [23]. As the drying times are determined experimentally, numerical drying models are applied to evaluate the drying process parameters, moisture transfer parameters, and moisture content distributions. Forced convection drying of moist objects was numerically modeled by Kaya et al. [24], where the computational predictions shown that the convective heat and mass transfer coefficients in the upstream side of the cylindrical object are higher than those of the downstream side. Sahin and Dincer [25] proposed a graphical method to estimate the drying moisture transfer parameters and drying times in a quick and efficient manner. The thermogravimetric analysis technique based research, to determine the moisture diffusivity of red apples at high temperatures, was performed by Feng et al. [26]. A two-dimensional numerical analysis of heat and moisture transfer during drying of a cylindrical object was performed by Hussain and Dincer [27], who determined that the moisture gradient was higher in the early drying period and as drying progresses, the moisture gradient remained almost steady. Sahin et al. [28] analytically investigated drying of multidimensional food products and developed a simple method to determine the drying times. Heat and mass transfer coefficients of air chilling and storage of solid food products, for the cases of solids of more complex shapes, were reviewed by Kondjoyan [29]. As Dincer and Hussain [30] developed new Biot number–Dincer number (Bi–Di) correlation for drying applications, microwave drying of sphere, cylinder, half-cylinder, and rectangular prism shaped particles, suspended in an air stream, was considered by Araszkiewicz et al. [31]. McMinn and Magee [32] studied the effects of air velocity and temperature on the drying rate and investigated the kinetics of moisture transport in potato cylinders. Monolayer moisture contents of okra were evaluated by Gogus and Maskan [33] for the drying temperature range of $60-80\,^{\circ}C$. They not only determined the augmentation of effective diffusivity with increasing temperature but also shown that the computed effective diffusivity data had Arrhenius type temperature dependence. Panagiotou et al. [34] retrieved and analyzed a wide collection of moisture diffusivity values, for various foods, from the recent publications. They also classified the data of more than 100 food materials in 11 categories.

The open literature clearly displays the strong need to study the boundary layer development and heat and mass transfer behavior of CCs that are exposed to confined fluid flow. Although several thermofluid CC studies exist in the literature, they are limited to either fluid flow, or fluid flow and heat transfer, or heat and mass transfer. Even though the heat transfer rates are significantly characterized by fluid flow and boundary layer development, and mass transfer coefficients by those of heat transfer, the open literature cannot offer any publication, studying the linkage of hydrodynamic boundary layer development and mass transfer for CCs. The present study aims (i) to develop a complete overview and to bridge the gap between the laminar boundary layer development,

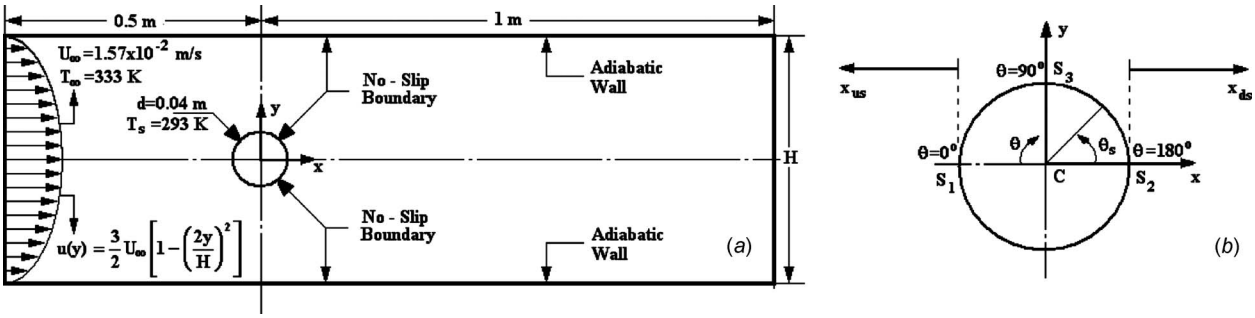

Fig. 1 (*a*) Flow domain around the cylinder and (*b*) the coordinate system

heat transfer rates and mass transfer behavior of CCs in confined flows, and (ii) to establish the impact of blockage on mass transfer mechanism for wide ranges of blockage ratios and moisture diffusivities. The laminar fluid flow and boundary layer development aspects are discussed through streamlines, velocity profiles, separation phenomena, pressure, and friction coefficients. The heat transfer analysis are presented by temperature profiles/contours and Nusselt numbers. The mass transfer results are given in terms of mass transfer coefficients, overall drying times, local drying schemes, and isomoisture contours within the CC.

2 Theoretical Background

2.1 Governing Equations. Figure 1 schematically shows the geometry and the relevant dimensions considered in the analysis. As given in Fig. 1(*a*), on either side of the center of the cylinder, two adiabatic channel walls are placed at a distance of H/2. No-slip boundary condition is applied both to the cylinder surface and to the adiabatic channel walls. A fixed two-dimensional circular cylinder with diameter d is maintained at a constant temperature of T_s. Air enters the duct with a fully developed laminar velocity profile of $u(y)=(3/2)U_\infty[1-(2y/H)^2]$ at a temperature of T_∞, where U_∞ is the average velocity of air at the duct inlet. Additionally, Fig. 1(*b*) displays the geometric notation, adapted for the fluid and heat-mass transfer investigations. As the surface points of S_1, S_2, and S_3 stand for the angular positions of $\theta=0$, 180, and 90 deg, the starting points of the upstream and downstream directions are S_1 and S_2, respectively.

Incropera and De Witt [35] reported that, according to the fundamental fluid mechanics theory, fluid flow around CC remains laminar up to the cylinder Reynolds number of $Re_d \leq 2\times10^5$. Flows with blockage were recently under the inspection of Sahin and Owens [6] and Rehimi et al. [7], where both of the works aimed to investigate the appearance of von Karman vortices and wake instability. As Sahin and Owens [6] recorded the neutral stability as $Re_d \approx 100$ for the blockage range of $\beta=0.333-0.800$, Rehimi et al. [7] evaluated the critical Reynolds number as $Re_d=108$. Since the focus of the present work is to investigate the laminar boundary layer development, heat transfer rates, and mass transfer behavior of CCs in confined flows, the computational analysis is carried out at the constant cylinder Reynolds number of $Re_d=40$, which is not only consistent with the laminar range of [35] but also sufficiently below the critical Reynolds numbers of Refs. [6,7]. Besides, the channel flow aspect of the problem is structured in the computations by adapting the duct height (H) in accordance with the level of blockage ratio ($\beta=d/H$). By simultaneously considering the traditional channel flow critical Reynolds number of Re=2300 [35], for the blockage ratio range of $\beta=0.200\rightarrow0.800$, duct height values are decided as $H=200\rightarrow50$ mm (Fig. 1(*a*)), where the consequent Reynolds number range for the channel flow becomes $Re_{ch}=400\rightarrow100$. Being compatible with these definitions, the fluid flow and heat transfer section of the present problem is structured on incompressible and constant fluid and thermal property characteristics and carried out in steady ($\partial/\partial t=0$) and two-dimensional fluid domain. Under these conditions, equations governing the two-dimensional laminar flow are given in the master Cartesian coordinate system as follows.

For continuity,

$$\frac{\partial u}{\partial x}+\frac{\partial v}{\partial y}=0 \tag{1}$$

For momentum,

$$\rho\left(u\frac{\partial u}{\partial x}+v\frac{\partial u}{\partial y}\right)=-\frac{\partial P}{\partial x}+\mu\left(\frac{\partial^2 u}{\partial x^2}+\frac{\partial^2 u}{\partial y^2}\right) \tag{2a}$$

$$\rho\left(u\frac{\partial v}{\partial x}+v\frac{\partial v}{\partial y}\right)=-\frac{\partial P}{\partial y}+\mu\left(\frac{\partial^2 v}{\partial x^2}+\frac{\partial^2 v}{\partial y^2}\right) \tag{2b}$$

For energy,

$$u\frac{\partial T}{\partial x}+v\frac{\partial T}{\partial y}=\alpha\left(\frac{\partial^2 T}{\partial x^2}+\frac{\partial^2 T}{\partial y^2}\right) \tag{3}$$

Although the hydrodynamic and thermal characteristics around the CC are steady, the moisture content inside the CC will decrease with time due to the drying role of the forced convection acting on the CC surface. It is also certain that the moisture level will not only vary in time but it is also location dependent within the CC. Due to these scientific prospects, moreover to accomplish the aims of the mass transfer section of the present research, the mass transfer mechanism, inside the dried object, is characterized by the two-dimensional moisture transfer equation of Eq. (4), with the assumption that the shrinkage or deformation of the material during drying is negligible.

$$\frac{1}{D}\frac{\partial M}{\partial t}=\frac{1}{r}\frac{\partial M}{\partial r}+\frac{\partial^2 M}{\partial r^2}+\frac{1}{r^2}\frac{\partial^2 M}{\partial \theta^2} \tag{4}$$

2.2 Boundary Conditions. In the fluid flow and heat transfer investigations, no-slip boundary condition (u=v=0) is applied to the channel walls and to the cylinder surface. As the cylinder surface is kept at constant temperature (T_s), channel walls are considered as adiabatic. A fully developed duct flow velocity profile and a freestream temperature (T_∞) are employed at the inlet; exit pressure is taken as atmospheric.

In the mass transfer analysis, an initial condition (Eq. (5*a*)) is assigned to the dried object. As the two boundary conditions in the radial direction are located at the center (Eq. (5*b*)) and surface (Eq. (5*c*)), those for the angular direction are both at $\theta=0=2\pi$ (Eqs. (5*d*) and (5*e*)).

$$M(r,\theta,0)=M_i \tag{5a}$$

$$\frac{\partial M(0,\theta,t)}{\partial r}=0 \quad \text{at} \quad r=0 \tag{5b}$$

$$-D\frac{\partial M(R,\theta,t)}{\partial r} = h_m(M - M_a) \quad \text{at} \quad r = R \tag{5c}$$

$$M(r,0,t) = M(r,2\pi,t) \tag{5d}$$

$$\frac{\partial M(r,0,t)}{\partial \theta} = \frac{\partial M(r,2\pi,t)}{\partial \theta} \tag{5e}$$

2.3 Parameter Definitions. Not only to describe the flow type and identify the considered scenarios but also to interpret the evaluated outputs in common scientific notation, the following dimensionless variables and parameters are used:

$$Re_d = \frac{\rho U_\infty d}{\mu} \tag{6a}$$

$$\beta = \frac{d}{H} \tag{6b}$$

$$C_p = \frac{P_\theta - P_\infty}{1/2\rho U_\infty^2} \tag{6c}$$

$$C_f = \frac{\tau_s}{1/2\rho U_\infty^2} \tag{6d}$$

$$\zeta = \frac{T - T_s}{T_\infty - T_s} \tag{6e}$$

$$-k\left.\frac{\partial T}{\partial n}\right|_s = h_\theta(T_s - T_a) \tag{6f}$$

$$Nu_\theta = \frac{h_\theta d}{k} \tag{6g}$$

$$Nu_{ave} = \frac{1}{2\pi}\int_0^{2\pi} Nu_\theta d\theta \tag{6h}$$

$$h_m = h_\theta\left(\frac{DLe^{1/3}}{k}\right) \tag{6i}$$

$$\phi = \frac{M - M_a}{M_i - M_a} \tag{6j}$$

where Re_d is the cylinder Reynolds number, β is the blockage ratio, C_p and C_f are the pressure and friction coefficients, ζ is the dimensionless temperature, h_θ is the local convective heat transfer coefficient, Nu_θ and Nu_{ave} are the local and average Nusselt numbers, h_m is the mass transfer coefficient, and ϕ is the dimensionless moisture content.

2.4 Computational Methods. Computational analyses are carried out in two-different platforms. As the fluid flow and heat transfer simulations are performed with ANSYS-CFX [36], moisture transfer mechanism is taken into consideration by a new alternating direction implicit (ADI) method based software, developed by the authors.

ANSYS-CFX applies the element-based finite-volume method and scalably adopts the multigrid solver to the defined flow domain. Since the overall error in CFD calculations is mainly a combination of grid density and iteration number (or convergence criterion), several successive runs are performed for each individual blockage case to ensure that the numerical outputs are free of the roles of computational items. Table 1 displays a summary of these tests for the four blockage cases of β=0.200, 0.333, 0.571, and 0.800 in terms of the fluid flow and heat transfer parameters that are the primary concerns of the present research. For the complete set of scenarios investigated, a convergence criterion of 1×10^{-7} is used to certain negligibly small iteration errors. Moreover, to predict the velocity and temperature gradients sensitively, refined mesh size is employed in the neighborhood of the solid boundaries (Fig. 1) with the expansion factor of 1.1 (Fig. 2). Since the initial computations indicated stronger gradients in higher blockage cases, to be able to detect the variations with minor geometric steps, the applied number of overall elements is increased accordingly.

Table 1 Grid node effects on fluid flow and heat transfer parameters

β	No. of nodes	$(P_s)_{\theta=0}$ (Pa)	$(\tau_s)_{max}$ (Pa)	Nu_{ave}
0.200	438,732	0.00033	0.00013	3.822
	487,462	0.00041	0.00014	3.697
	503,978	0.00046	0.00014	3.663
	514,318[a]	0.00047	0.00014	3.659
0.333	337,216	0.00081	0.00019	4.172
	408,358	0.00084	0.00019	4.082
	423,137	0.00086	0.00020	4.055
	431,216[a]	0.00086	0.00020	4.051
0.571	293,517	0.00220	0.00032	5.140
	354,713	0.00231	0.00036	5.019
	364,872	0.00233	0.00036	4.977
	374,723[a]	0.00234	0.00037	4.968
0.800	287,437	0.01293	0.00165	6.730
	346,831	0.01321	0.00177	6.547
	358,195	0.01329	0.00182	6.521
	367,048[a]	0.01332	0.00184	6.513

[a]Optimum grid nodes.

The ADI method is a finite difference method for solving parabolic and elliptic partial differential equations in two or more dimensions. For the cylindrical coordinate diffusion equation (Eq. (4)), the idea in ADI is to split the finite difference equations into two: one with the r-derivative (Eq. (7*a*)) and the next with the θ-derivative (Eq. (7*b*)), both taken implicitly.

$$M_{i,j}^{n+1}\left(\frac{2}{D\Delta t} + \frac{2}{\Delta r^2}\right) - M_{i+1,j}^{n+1}\left(\frac{1}{2r\Delta r} + \frac{1}{\Delta r^2}\right) + M_{i-1,j}^{n+1}\left(\frac{1}{2r\Delta r} - \frac{1}{\Delta r^2}\right) = M_{i,j}^{n+1/2}\left(\frac{2}{D\Delta t} - \frac{2}{r^2\Delta\theta^2}\right) + M_{i,j+1}^{n+1/2}\left(\frac{1}{r^2\Delta\theta^2}\right) + M_{i,j-1}^{n+1/2}\left(\frac{1}{r^2\Delta\theta^2}\right) \tag{7a}$$

$$M_{i,j}^{n+1/2}\left(\frac{2}{D\Delta t} + \frac{2}{r^2\Delta\theta^2}\right) - M_{i,j+1}^{n+1/2}\left(\frac{1}{r^2\Delta\theta^2}\right) - M_{i,j-1}^{n+1/2}\left(\frac{1}{r^2\Delta\theta^2}\right) = M_{i,j}^{n}\left(\frac{2}{D\Delta t} - \frac{2}{\Delta r^2}\right) + M_{i+1,j}^{n}\left(\frac{1}{2r\Delta r} + \frac{1}{\Delta r^2}\right) + M_{i-1,j}^{n}\left(\frac{1}{\Delta r^2} - \frac{1}{2r\Delta r}\right) \tag{7b}$$

$$\lambda = \frac{D\Delta t}{(\Delta r^2 + \Delta r^2\Delta\theta^2)} \tag{7c}$$

The solution procedure of Eq. (4) is carried out in conjunction with the initial and boundary conditions of Eq. (5). According to the Lewis analogy [35], mass transfer coefficient (h_m) is significantly related (Eq. (6*i*)) with the convective heat transfer coefficient (h_θ) and characterizes the amount of moisture swept away from the cylinder surface. By obtaining the h distribution on the cylinder surface from ANSYS-CFX solver, h_m variation is also gen-

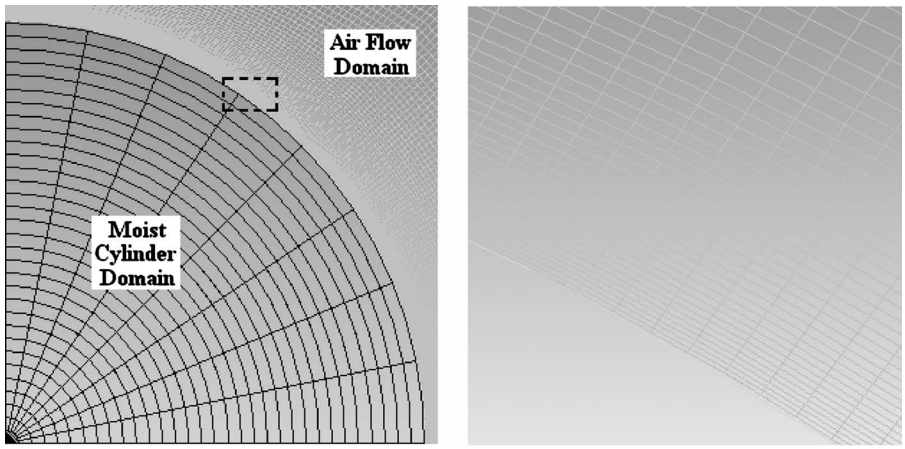

Fig. 2 Grid resolution in and around the cylinder interface

erated. Since computations showed negligible changes with denser meshes, diffusion investigations are performed with the mesh density of 31×31. Moreover, similar to the works of Kaya et al. [24,37], the convergence of ADI is guaranteed with the under-relaxation parameter of $\lambda = 0.5$. As λ is dependent on moisture diffusivity (Eq. (7*c*)), the time step (Δt) in the computations is regulated in accord with the level of diffusivity. Thus, in higher diffusivity cases, adopting lower time steps resulted in extended run-times.

3 Results and Discussion

In order to conduct the study, some physical, hydrodynamic, and thermal data are gathered from the recent publications [4,5,7,8,14,21,23,24,26,27,34,38,39]. The computational studies on the laminar hydrodynamic and thermal boundary layer development and mass transfer characteristics of a circular cylinder are carried out at the constant Reynolds number of $Re_d = 40$, with the average inlet air velocity and cylinder diameter values of $U_\infty = 1.57 \times 10^{-2}$ m/s and $d = 0.04$ m, respectively. Additionally, inlet air temperature, cylinder temperature, and moisture contents of air and cylinder are chosen as $T_\infty = 333$ K, $T_s = 293$ K, $M_a = 0.1$ kg/kg, and $M_{cyl} = 3$ kg/kg, respectively, where these numbers are similar to those of Refs. [8,14,21,23,24,26,27,38,39]. To develop a complete overview on the interactions of hydrodynamic and thermal characteristics with mass transfer behavior, extensive numerical analysis are performed by systematically varying the blockage ratio (β) and moisture diffusivity (D). As the blockage ratio range is selected as $\beta = 0.200 - 0.800$ being similar to those of Griffith et al. [4], Chakraborty et al. [5], Rehimi et al. [7], and Sen et al. [8]; the moisture diffusivity limits are adopted from the real time data of Panagiotou et al. [34] as $D = 1 \times 10^{-8} - 1 \times 10^{-5}$ m^2/s. Fluid flow and heat transfer characteristics are discussed under Secs. 3.1.1 and 3.1.2. As upstream and downstream streamlines, temperature contours, velocity, and temperature profiles are related to the flow domain, hydrodynamic, and thermal boundary layer mechanism on the cylinder surface are enlightened through pressure coefficients, shear stresses, Nusselt numbers, and separation phenomena. Mass transfer results are demonstrated in Sec. 3.2.1 (mass transfer coefficients, drying times), Sec. 3.2.2 (local drying characteristics), and Secs. 3.2.3 and 3.2.4. In Sec. 3, to identify not only the novelty of the findings but also the originality of the work, cross-correlating the evaluations with blockage ratios, moisture diffusivities, and drying times is applied as the presentation strategy.

3.1 Fluid Flow and Heat Transfer Characteristics

3.1.1 Flow Domain Results. Through Fig. 3, it is aimed not only to demonstrate the streamline formation (Fig. 3(*a*)) and temperature contours (Fig. 3(*b*)) around the cylinder but also to further validate the evaluated computational outputs. Numerical outputs, for the streamline and temperature contour formation, come out to be completely symmetric, appearing as a mirror image, having the centerline as the symmetry axis. Indeed this symmetric behavior originates mainly due to two scientific issues: (i) The fluid flow around the cylinder is in the laminar regime and (ii) the centerline of the cylinder coincides with the midplane of the adiabatic duct walls. Thus, both the streamline and temperature contour discussions are carried out in the half fluid domain for the three sections of the upstream, the throat, and the downstream. It can be seen from Fig. 3(*a*) that in the upstream region of the cylinder, centerline streamlines deviate from their route easily in the low β range of $\beta = 0.200 - 0.333$. However, with the increase of blockage ($\beta = 0.571 - 0.800$), they are hydrodynamically forced to keep their route up to the neighborhood of the cylinder surface. The disciplined approach result in smoothly moving upstream streamlines, having tangent paths to the front face of the cylinder and can be further expected to cause significantly augmented static pressure and heat transfer data in the considered region. It can additionally be said that the dominant fluid contact with the cylinder surface can be an apparent source for high friction rates. In the throat, the fluid attains the maximum velocity values computed for the complete flow domain, such that as the maximum velocity values computed for $\beta = 0.200$ and $\beta = 0.333$ are $U_{th\text{-}max} = 2.70 \times 10^{-2}$ m/s ($U/U_\infty = 1.722$) and $U_{th\text{-}max} = 3.27 \times 10^{-2}$ m/s ($U/U_\infty = 2.083$), respectively, the corresponding numbers for $\beta = 0.571$ and $\beta = 0.800$ are $U_{th\text{-}max} = 5.05 \times 10^{-2}$ m/s ($U/U_\infty = 3.217$) and $U_{th\text{-}max} = 1.09 \times 10^{-1}$ m/s ($U/U_\infty = 6.943$). The rise in the $U_{th\text{-}max}$ values is expected due to the narrowing style of the flow domain between the duct wall and the cylinder surface. These numbers, and the continuity theory, further put forward that, in addition to producing augmented $U_{th\text{-}max}$ values, narrower throats result in fuller velocity profiles as well. Indeed, both the accelerated fluid movement and the strictly attaching boundary layer formation on the cylinder surface (due to fuller velocity profiles) delay the separation point toward downstream (zoomed plots in Fig. 3(*a*)). The separation angles of $\theta_s = 54.10$, 50.20, 41.98, and 37.30 deg for $\beta = 0.200$, 0.333, 0.571, and 0.800, respectively, are obtained by the computations, where similar to Refs. [5,8,36–39], the separation locations (θ_s) are measured in the counterclockwise direction,

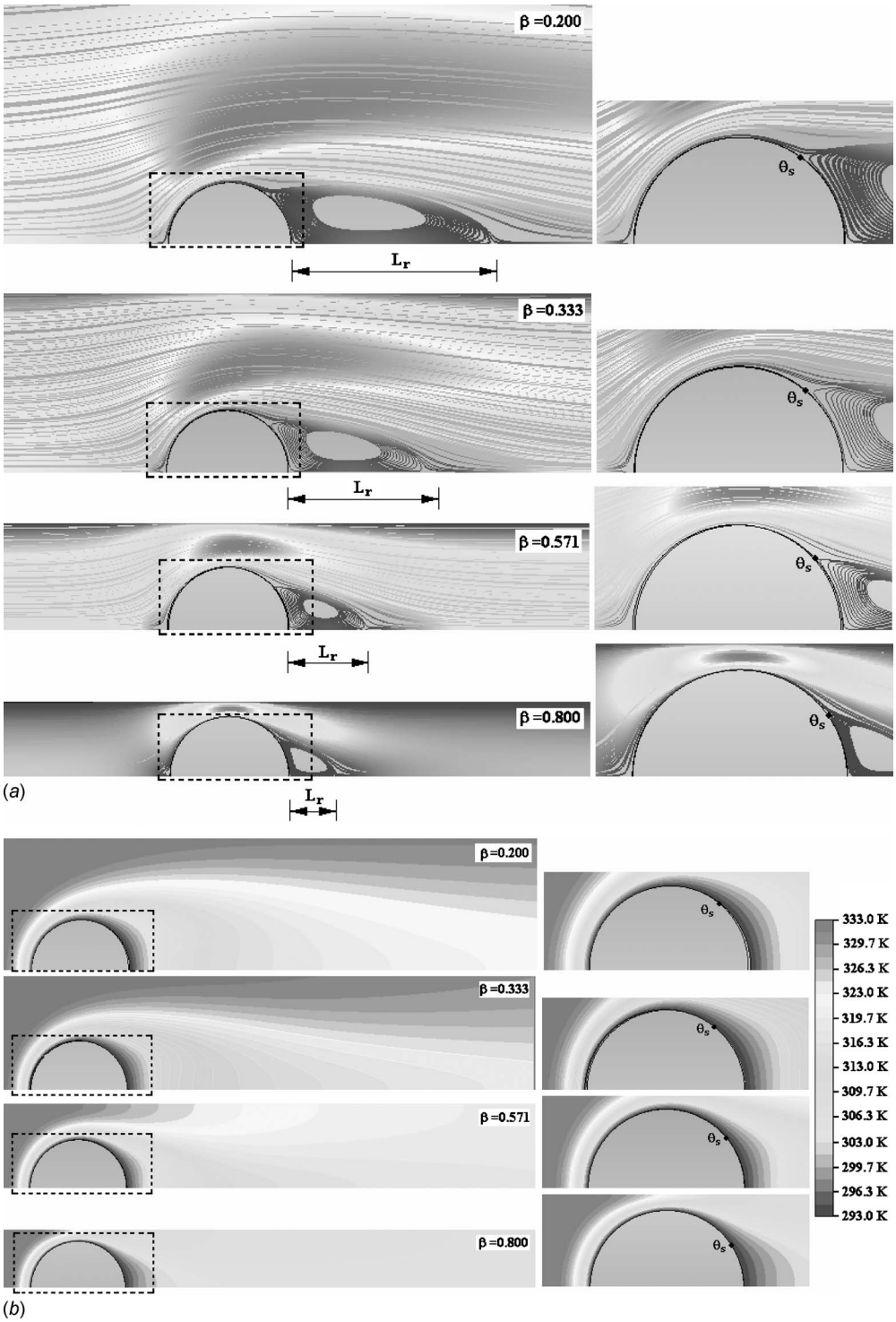

Fig. 3 (*a*) **Streamline formation and** (*b*) **temperature contours around the cylinder for the blockage ratio range of** β**=0.200–0.800**

with the origin of S_2 (Fig. 1(*b*)). Several experimental and numerical works considered flows around circular cylinders without blockage. The unconfined flow, for the specific case of Re=40, was investigated by Refs. [5,40–43], where their evaluations on the separation location were relatively comparable being in the range of θ_s=53.1–53.8 deg. Among the considerably fewer work on flows with blockage, Chakraborty et al. [5] and Sen et al. [8] handled the Re=40 flow around CCs. Either of the research computationally determined the shift of separation toward downstream. As the representative outputs were $\theta_s \approx 53$, 50, 48, and 45 deg for β=0.200, 0.333, 0.500, and 0.650 in Ref. [5], those of Ref. [8] were reported as $\theta_s \approx 52$, 46, 37.5, and 26.5 deg for β=0.200, 0.333, 0.500, and 0.800, respectively. It can be seen that, especially for flows with high blockage, a scientific agreement is not available between Refs. [5,8]; the present findings relatively resemble those of Chakraborty et al. [5]. On the other hand, the present separation

finding (θ_s=54.10°) at the lowest blockage case (β=0.200) is comparable with the identical flow condition data of both Ref. [5] ($\theta_s \approx 53°$) and Ref. [8] ($\theta_s \approx 52°$). It must additionally be pointed out that the separation location of β=0.200 is close to the unconfined flow reports (θ_s=53.1–53.8 deg) of Refs. [5,40–43]. This convergence indicates that the impact of blockage loss strength for $\beta \leq 0.200$, where similar evaluations were as well achieved by Chakraborty et al. [5] and Sen et al. [8]. The onset of the downstream flow domain can be marked by θ_s points, where the following is a vortex structure just at the downstream vicinity of the cylinder (zoomed plots in Fig. 3(*a*)). Figure 3(*a*) indicates that the occupied region of the vortex becomes contracted with higher β. Specifically speaking, the lengths of the recirculation zones are computed as $L_r = \sim 63.9$ mm (β=0.200), $L_r = \sim 47.3$ mm (β=0.333), ~26.9 mm (β=0.571), and ~16.7 mm (β=0.800), indicating that blockage negatively affects the influential domain and the strength of the downstream vortex system. Similar findings on shorter recirculation zones with higher blockage were also reported by Griffith et al. [4] for the blockage range of β=0.050–0.900, Chakraborty et al. [5] for the blockage range of β=0.050–0.650, and Sen et al. [8] for the blockage range of β=0–0.800. Further detailed results on the hydrodynamic characteristics and momentum transfer essentials for the upstream, throat, and downstream sections are presented in Figs. 4(*a*) and 5(*a*).

Throat and downstream temperature contours are given in Fig. 3(*b*). The computational analysis indicated for high blockage cases that the hot fluid domains not only get closer to the cylinder surface but also cover thinner regions; moreover, the forced contact of the hot fluid with the cylinder gives way to higher heat transfer rates. The zoomed plots of Fig. 3(*a*) clearly identify that with the increase of blockage the thermal boundary layer gets thinner up to the separation point (θ_s). The thickening attitude of thermal boundary layers beyond the separation point in the complete blockage cases can also be seen from Fig. 3(*b*). This finding is as well in agreement with the recirculation zone length values of Fig. 3(*a*), indicating the significant interactions of hydrodynamic and thermal characteristics. Buyruk et al. [17] reported the similar impact of β on the isotherm structure in the wake of a cylinder. In the flows with β=0.200–0.571, the isotherm contours become similar toward θ=180 deg (zoomed plots of Fig. 3(*b*)), where this evaluation is an indicator for comparable heat transfer rates in the neighborhood of θ=180 deg. However, at the highest blockage flow of β=0.800 the thermal boundary layer displays a thicker structure, when compared with the milder blockage cases of $\beta < 0.800$. The essentials of this evaluation can be associated with two issues: (i) High backward velocity values exist at β=0.800 and (ii) the narrowing nature of the downstream vortex system disturbs the boundary layer and weakens the fluid-solid contact. Further detailed discussions on the thermal characteristics and heat transfer essentials for the upstream, throat, and downstream regions are provided through Figs. 4(*b*) and 5(*b*).

The dimensionless velocity and temperature profiles in the upstream domain of the cylinder are presented in Figs. 4(*a*) and 4(*b*) for the blockage ratio range of β=0.200–0.800. Figure 4(*a*) shows that the role of the cylinder on the hydrodynamic behavior of the flowing air becomes apparent at closer sections at the front side of the cylinder for high β cases. Such that for β=0.200, 0.333, 0.571, and 0.800, the dimensionless velocity values are computed as U/U_∞=0.26, 0.34, 0.44, and 0.53, respectively, at the centerline of $x_{us}=5\times10^{-3}$ m. This finding indicates that, due to the late hydrodynamic response of the flow domain at higher β scenarios, flowing air decelerates more rapidly to zero toward the stagnation point ($x_{us5} \rightarrow x_{us1}$), resulting in an augmented momentum velocity in the neighborhood of the cylinder. For x_{us}=0 m, it can be seen from Fig. 4(*a*) that on the cylinder projection lines ($y = \pm 0.02$ m), the dimensionless velocity values (U/U_∞) rise at higher blockage ratios (β). This finding can be related to the downstream movement of the separation point (θ_s) at high β (Fig. 3). On the other hand, the velocity profiles attained at x_{us}=0 m for β=0.200–0.800 resemble a fuller form with the increase of β. Indeed, this outcome, together with the presented streamlines of Fig. 3(*a*), point out thinner boundary layer formations at higher blockage ratios. Additionally, the computations clarified the U/U_∞ ranges at $y = \pm 0.02$ m as 1.05→1.10, 1.24→1.33, 1.41→1.66, and 1.35→2.01 ($x_{us5} \rightarrow x_{us1}$) for β=0.200, 0.333, 0.571, and 0.800, clarifying the rise of velocity values at higher β cases. Moreover, the wider ranges at high β can be attributed to the augmented momentum activity described above. It can also be seen from Fig. 4(*a*) that the order of the upstream velocity profiles reverses at the intersection points. The reverse locations are computed to occur at $y_{rev} = \pm \sim 0.0171$ m ($U/U_\infty = \sim 0.932$), $y_{rev} = \pm \sim 0.0163$ m ($U/U_\infty = \sim 1.076$), $y_{rev} = \pm \sim 0.0148$ m ($U/U_\infty = \sim 1.229$), and $y_{rev} = \pm \sim 0.0126$ m ($U/U_\infty = \sim 1.251$) for β of 0.200, 0.333, 0.571, and 0.800, respectively. The decrease of y_{rev}, the rise of the corresponding U/U_∞ values, and the significantly interacting streamlines with the cylinder (Fig. 3(*a*)) at higher β are clear confirmations for thinner boundary layers and higher momentum rates and trustable evidences for higher frictional activity and heat transfer rates at the cylinder surface.

Figure 4(*b*) demonstrates the variation of dimensionless temperatures (ζ, Eq. (6*e*)), upstream of the cylinder, for the blockage ratio range of β=0.200–0.800. It can be seen from the figure that significant decreases in temperature are evaluated while approaching the stagnation point of the cylinder (x_{us}=0 m and y=0 m). The role of blockage is determined to be more sensible in the flow domain of $x_{us}=0-5\times10^{-3}$ m. Within this domain, higher blockage resulted in higher ζ values, which is completely in harmony with the temperature contours of Fig. 3(*b*). In other words, similar to the hydrodynamic boundary layer development, the thermal boundary layer also attains lower thickness values at higher blockage. This cannot only be considered as a matching validation of the hydrodynamic and thermal results but also strengthened the discussions on augmented heat transfer activity at higher β. Computations further indicated that as the centerline dimensionless temperature range is ζ=0.049→0.039 (β=0.800→0.200) at $x_{us}=2\times10^{-4}$ m, and the corresponding values for the stagnation point (x_{us}=0 m) are ζ=0.006→0.005. The narrowing nature of the dimensionless temperature range points out that the impact of blockage on heat transfer rates reduces in the neighborhood of the cylinder, especially at the stagnation point (y=0 m and θ=0 deg).

Figures 5(*a*) and 5(*b*) show the dimensionless downstream velocity and temperature profiles for the blockage ratio range of β=0.200–0.800. To generate a visual comparison opportunity, velocity profiles for the same flow domain of $x_{ds}=0-5\times10^{-3}$ m are demonstrated in Fig. 5(*a*) for the complete β range investigated. In addition to the presented vortex structure in Fig. 3(*a*), through Fig. 5(*a*), it is aimed to provide a deeper discussion on the downstream velocities, strength of the vortices, and the role of the downstream momentum transfer. As can be seen from Fig. 5(*a*), regardless of the level of blockage ratio, backflow ($U/U_\infty < 0$) exists in the downstream section of the cylinder. However, since the strength of the vortex structure can explicitly be defined not only by the magnitude of the backflow but also with the extension of the flow domain that is influenced by the backflow regime, the impact of blockage on the vortex strength comes out to be significantly important. The computations put forward a rise in the backflow velocity values with higher β. Such that as the centerline dimensionless velocity values at $x_{ds}=5\times10^{-3}$ m are computed as U/U_∞=−0.039 and U/U_∞=−0.052 for β=0.200 and β=0.333, respectively, for the same location the corresponding records are evaluated as U/U_∞=−0.094 and U/U_∞=−0.131 for β=0.571 and β=0.800. From the point of momentum transfer around the separation point, it can be said that the growth of the backflow values is highly characterized by the comprehensively augmented throat

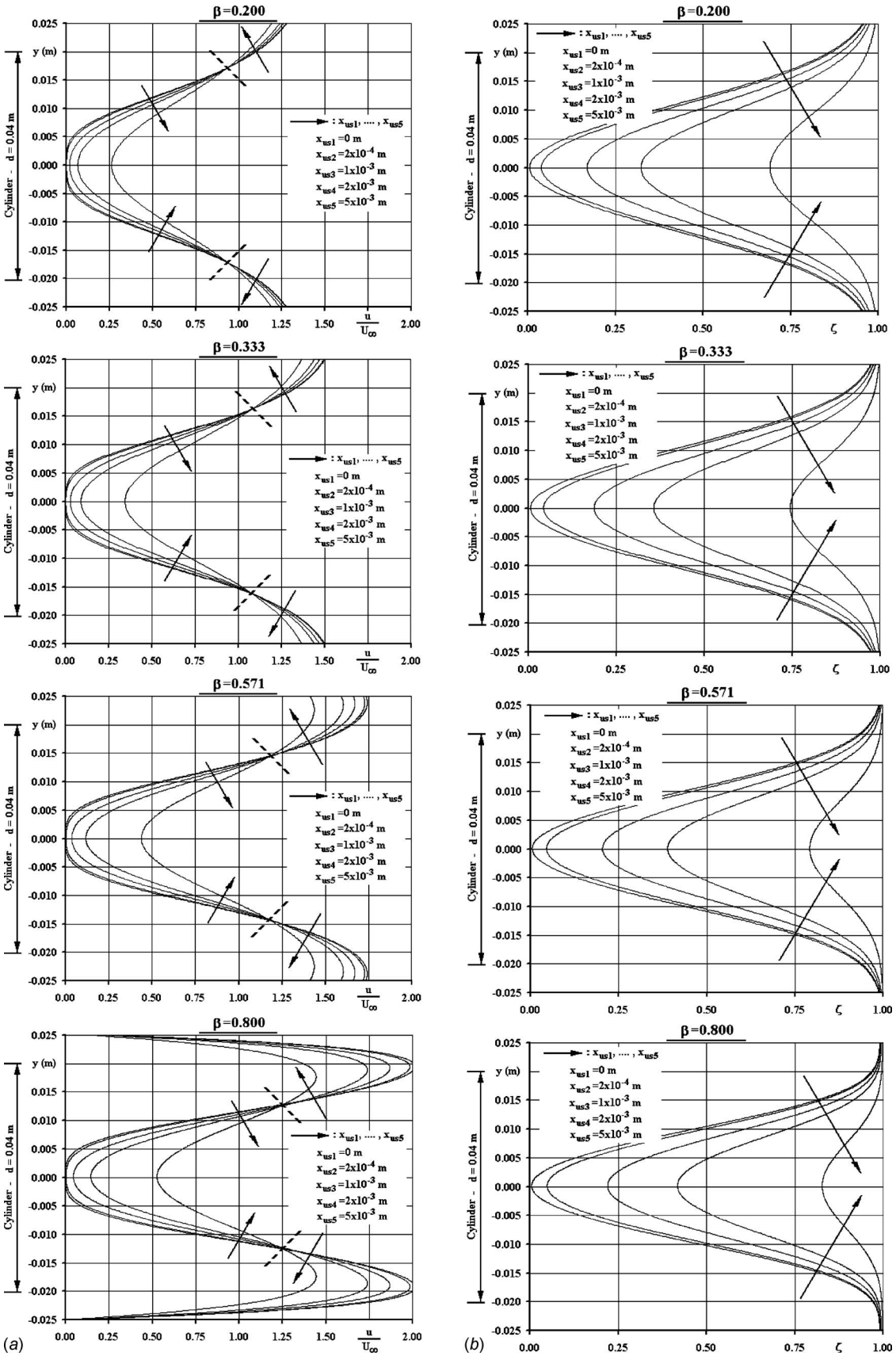

Fig. 4 Dimensionless (*a*) velocity and (*b*) temperature profiles at the upstream of the cylinder for the blockage ratio range of β=0.200–0.800

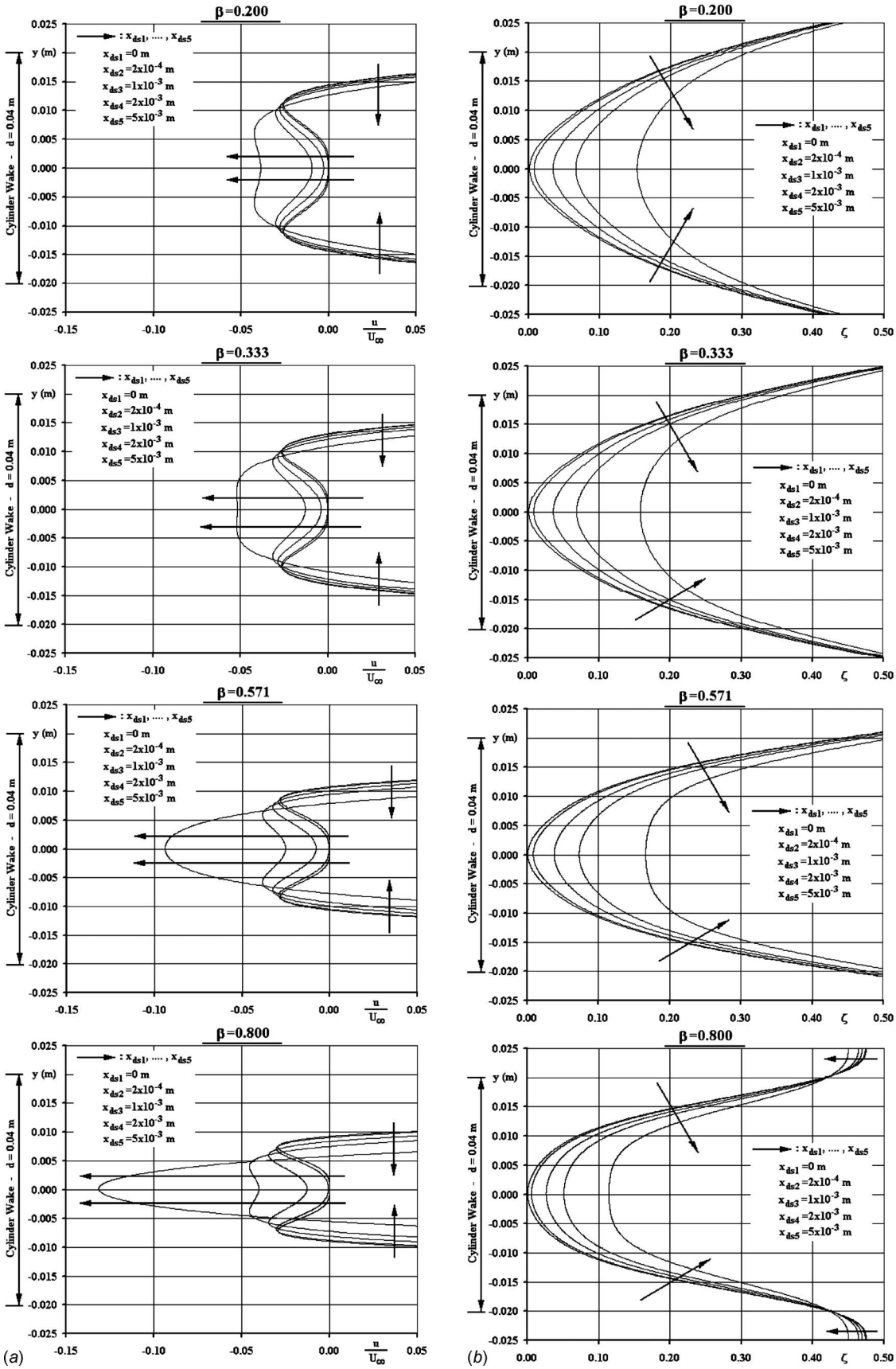

Fig. 5 Dimensionless (*a*) velocity and (*b*) temperature profiles at the downstream of the cylinder for the blockage ratio range of β=0.200–0.800

velocity values of Fig. 4(*a*) at high β. As the downstream shift of θ_s with high blockage ratio (Fig. 3(*a*)) is an outcome of the elevated momentum of fluid motion supporting the boundary layer development by suppressing the negative pressure gradient effects in the decelerating fluid domain, the subsequent hydrodynamic structure is as well characterized by the level of the throat velocity values. In other words, it can be termed as follows: Higher blockage not only augments the throat momentum transfer but also moves the separation point downstream. Not only from the schematic point of view but also according to the role of blockage on the wake (downstream) velocity profiles, the present evaluations match with the circular cylinder findings of Sen et al. [8] (β=0–0.800) and Buyruk et al. [17] (β=0.18–0.47). The downstream velocity profiles additionally verify the determinations on the narrower vortex domain (Fig. 3(*a*)) at high β with the specific width figures of $y=\pm 0.0191 \rightarrow \pm 0.0176$ m, $y=\pm 0.0160 \rightarrow \pm 0.0130$ m, $y=\pm 0.0124 \rightarrow \pm 0.0090$ m, and $y=\pm 0.0110 \rightarrow \pm 0.0064$ m ($x_{ds1} \rightarrow x_{ds5}$) for β=0.200, β=0.333, β=0.571, and β=0.800, respectively. The narrower vortex formation at high β, together with the continuity approach, can be regarded as a secondary factor on the rise of downstream backflow velocities.

The dimensionless downstream temperature profiles are given in Fig. 5(*b*). These results are significant not only to define the heat transfer characteristics in the downstream region of the flow domain but also to distinguish the role of vortex formation (Figs. 3(*a*) and 5(*a*)) on the heat transfer mechanism. The plot interprets for the investigated domain of $x_{ds}=0-5\times10^{-3}$ m that higher blockage ratio causes the fluid movement in the cylinder neighborhood to become hotter. As the isotherms of Fig. 3(*b*) point out, in the neighborhood of θ=180 deg and x_{ds}=0 m the dimensionless temperature values of the confined flow cases of β=0.200–0.571 resemble especially within the separated vortex domain of $x_{ds}=0-1\times10^{-3}$ m (Fig. 3(*a*)). The similar structure of the thermal layouts of β=0.200–0.571 cases is a trustable foresight for comparable heat transfer in the corresponding region. However, the high blockage of β=0.800 results in a unique temperature distribution when compared with those of the lower blockage cases. The lowest view of ζ at β=0.800 (Fig. 5(*b*)) in the complete blockage range results in a narrower temperature gap among the flow and cylinder, a mild temperature gradient, and lower heat transfer rates in that section of the cylinder surface. This outcome can scientifically be detailed by rationalizing the issue of downstream distance in conjunction with the recirculation length (L_r). As L_r is shown to become shorter with high β, the impact of blockage on the thermal activity of the separated domain comes into sight even in the neighborhood of the contact plane of the cylinder and in the downstream vortex system. On the other hand, the contrary evaluation can be set for low blockage scenarios with wider recirculation zones. These findings imply that besides demonstrating the impact of β on ζ, Fig. 5(*b*), as well presents the influence of downstream vortex formation on the flow temperature distribution. Besides, for the complete β range considered the stagnation point (θ=0 deg and x_{us}=0 m) dimensionless temperature values ($\zeta \approx 0.0055$) (Fig. 4(*b*)) are superior to those of the θ=180 deg and x_{ds}=0 m ($\zeta \approx 0.0012$) (Fig. 5(*b*)). This finding is a sign of advanced heat transfer at the upstream of the cylinder. This determination additionally puts forward that the momentum in the vicinity of the stagnation point has major potential, than the downstream vortex system, to bring about significantly augmented heat transfer rates.

3.1.2 Cylinder Surface Results. Figure 6 presents the angular variations of pressure coefficient (C_p), friction coefficient (C_f), and Nusselt number (Nu_θ) on the cylinder surface for the blockage ratio range of β=0.200–0.800. It can be seen from Fig. 6(*a*) that on the front face of the cylinder, the pressure coefficient values are considerably affected by the blockage ratio values, where C_p is determined to rise with β. At the stagnation point (θ=0°),

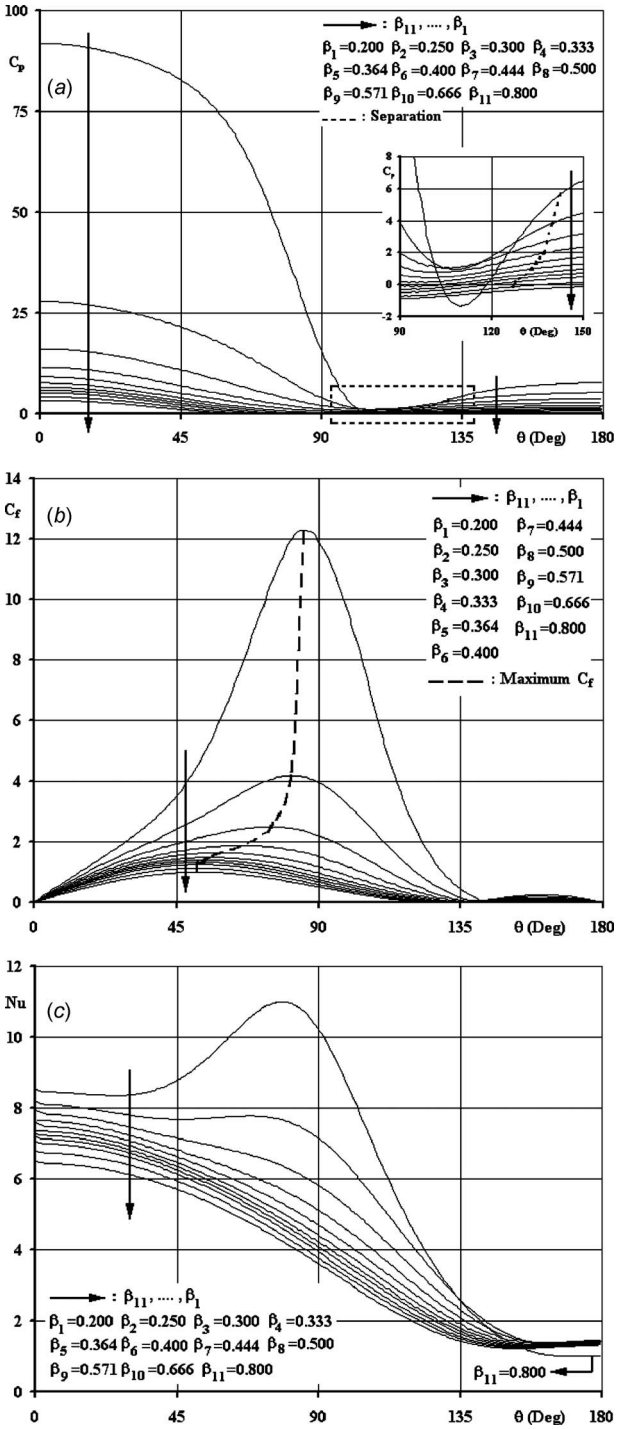

Fig. 6 Variation of (*a*) pressure coefficient, (*b*) friction coefficient, and (*c*) Nusselt number on the cylinder surface for the blockage ratio range of β=0.200–0.800

the highest blockage of β=0.800 creates a pressure coefficient of C_p=91.81, whereas the corresponding values for $\beta=0.500 \rightarrow 0.200$ appear as $C_p=11.51 \rightarrow 3.26$. Showing harmony with the present determinations, the rise of C_p with β was also reported by a few studies; such as the circular cylinder investigations of Chakraborty et al. [5] for $Re<200$ with β=0.05–0.65, Buyruk et al. [17] for $120<Re<390$ with β=0.18–0.47, Sharma and Eswaran [19] for $50<Re<150$ with β=0.10–0.50, Khan et al. [18] for laminar and turbulent flows with β=0.30–0.80, and the square cylinder work of Dhiman et al. [20] for $Re<45$ with β=0.125–0.25. Computations additionally indicated continuous

decreases in C_p toward the throat ($\theta=90°$). The drop in C_p is strictly dependent on the flow acceleration in the associated region; in other words, as the dynamic pressure rises, the contrary arises in the static pressure data. Numerical analysis indicates that the minimum C_p locations are positioned upstream of the separation points (θ_s). Indeed the gap among θ_s and θ_{C_p-min} becomes narrower at high β; such that as the θ_s-θ_{C_p-min} difference is 37.6 deg for $\beta=0.200$, it decreases down to 32.8 deg at $\beta=0.800$. In high β cases, the emergence of minimum C_p values at distant angular positions can be explained by the determinedly attaching boundary layer and delayed separation in these scenarios (Figs. 3(*a*) and 4(*a*)). Downstream of the separation location, Fig. 6(*a*) additionally puts forward an almost constant C_p domain, which is characterized and structured by the vortex regime, in other words the separated flow.

Angular variation of friction coefficient values is displayed in Fig. 6(*b*). It can be seen from the figure that, similar to the results of Chakraborty et al. [5], Khan et al. [18], and Dhiman et al. [20], C_f data are computed to rise with β on the complete cylinder surface. This augmentation can be attributed to the forced fluid contact and significantly interacting streamlines with the cylinder (Fig. 3(*a*)) and fuller velocity profiles (Fig. 4(*a*)) at high blockage cases. The location of maximum C_f are computed to shift downstream with high β, such that as θ_{C_f-max} is 51.5 deg at $\beta=0.200$, it becomes 85.4 deg at $\beta=0.800$. These values match with the maximum C_f location evaluations of Zukauskas and Ziugzda [44] ($\theta_{C_f-max}=\sim 50$ deg) for $\beta=0$ and that of Khan et al. [18] ($\theta_{C_f-max}=\sim 60$ deg) for $\beta=0.4$ case, however, slightly differ from the corresponding reports of Khan et al. [12] ($\theta_{C_f-max}=\sim 58$ deg) and Schonauer [45] ($\theta_{C_f-max}=\sim 57$ deg) for $\beta=0$. The performed analysis additionally puts forward a computational relation among the C_p and C_f variations: The θ_{C_f-max} points match the $\partial^2 C_p/\partial\theta^2=0$ locations. It can be said that maximum C_f are located at the angular points, where the trends in C_p curves reverse to attain the minimum C_p values. Figure 6(*b*) further clarifies the delay of separation with blockage and also the frictionless (no-shear) character in the corresponding domain.

The variation of Nusselt number on the cylinder surface is given in Fig. 6(*c*). The figure clearly puts forward the increase of Nusselt numbers; thus, surface heat transfer rates, with higher blockage, where similar findings were also reported by Bharti et al. [14], Buyruk et al. [17], Khan et al. [18], and Dhiman et al. [20]. Computational studies result in the average Nusselt numbers of $Nu_{ave}=6.51$, 4.97, 4.05, and 3.66 for the blockage ratio cases of $\beta=0.800$, 0.571, 0.333, and 0.200, respectively. For the specific case of Re=40, Biswas and Sarkar [41], Dennis et al. [43], Jafroudi and Yang [46], and Apelt and Ledwich [47] considered flows around circular cylinders without blockage and evaluated average Nusselt numbers in the narrow band of $Nu_{ave}=3.20-3.48$. The close agreement of the unconfined flow values of [41,43,46,47] with the present Nu_{ave} of 3.66 at $\beta=0.200$ strengthens the determination on the negligible impact of blockage for $\beta\leq 0.200$. Moreover, Khan et al. [18] reported the average Nusselt number for the blockage scenario of $\beta=0.200$ as $Nu_{ave}=3.44$, which is quite similar to the present corresponding finding ($Nu_{ave}=3.66$). Besides, the computed Nu_{ave} indicate the augmentation rates of 77.9% among the $\beta=0.800$ and $\beta=0.200$ cases, and 35.8% among the $\beta=0.571$ and $\beta=0.200$ scenarios. On the other hand, it can also be inspected from the figure that the impact of blockage on Nusselt numbers differs depending on the angular position. At the stagnation point, Nusselt numbers for the $\beta=0.800$, 0.571, 0.333, and 0.200 cases are evaluated as Nu=8.53, 7.94, 7.17, and 6.49, respectively, having the $Nu_{\beta=0.800}/Nu_{\beta=0.200}$ and $Nu_{\beta=0.571}/Nu_{\beta=0.200}$ ratios of 1.31 and 1.22. Except for the $\beta=0.800$ case, computations indicated the Nu to decrease in the angular direction, following the stagnation point. Moreover, the above defined ratios are determined as $Nu_{\beta=0.800}/Nu_{\beta=0.200}=1.53$ and 2.85, $Nu_{\beta=0.571}/Nu_{\beta=0.200}=1.23$ and 1.61 at the angular locations of $\theta=45$ and 90 deg, respectively. These records clearly put forward that the impact of blockage on heat transfer mechanism becomes significant toward the throat. This outcome can be enlightened by the close relation of the thermal and hydrodynamic structures. As was reported in Ozalp and Umur's [48,49] experimental studies for external flat and curved flows and in Ozalp's [50,51] computational investigations on internal microduct flows, thinner boundary layers provoke the heat transfer rates to rise. Similar outcomes were also announced by many other researchers both for internal and external flows [52,53]. High blockage based thinner boundary layer formation on the front face was clearly identified through the discussions concerning the role of blockage on the momentum transport and flow pattern (Figs. 3(*a*) and 4(*a*)). The present evaluations on the grow of heat transfer rates with high blockage cannot only be recognized with thinner boundary layer phenomena but can also be considered as a verification for the matching of hydrodynamic and thermal results. Figure 6(*c*) further points out the minimum heat transfer locations as being downstream of the separation points. The nearly constant temperature field in the downstream vortex domain (Fig. 5(*b*)) results in the almost constant heat transfer values in the angular domain of ~ 162 deg $<\theta<180$ deg. Besides, Fig. 6(*c*) further indicates for the cylinder surface section of ~ 162 deg $<\theta<180$ deg that the surface heat transfer rates of the blockage range $\beta=0.200-0.666$ are quite similar, which can be depended on the comparable combined impact of blockage and downstream vortex system on the heat transfer mechanism. But, as clarified in Fig. 3(*a*), the strength of the downstream vortex reduces at the highest blockage of $\beta=0.800$, which as a consequence negatively affects the heat transfer rates. On the other hand, being lower in magnitude, the influential region of the constant heat transfer values becomes narrower (~ 166 deg $<\theta<180$ deg), which can scientifically be linked to the thinner vortex formation at $\beta=0.800$ (Fig. 3(*a*)). It can be extracted from the point of back face heat transfer rates that as the $Nu_{\beta=0.800}/Nu_{\beta=0.200}$ ratio attains the values of 1.86 and 0.79 at $\theta=135$ and 180 deg, the corresponding values for $Nu_{\beta=0.571}/Nu_{\beta=0.200}$ emerge as 1.59 and 1.11. Since the throat ($\theta=90$ deg) ratios come out be superior on the complete cylinder surface, it can be concluded that the impact of boundary layer thinning is dominant to the role of the vortex structure on the heat transfer mechanism.

3.2 Mass Transfer Characteristics

3.2.1 Primary Findings. The mass transfer analysis within the circular cylinder, which is placed in a flow domain having a blockage ratio range of $\beta=0.200-0.800$, requires the knowledge about mass transfer coefficients on the cylinder surface. It is well known that [35] heat and mass transfer coefficients interrelate and in this work this relationship is implemented into the calculations with Eq. (6*i*), as was also applied by Kaya et al. [24]. The semilog plot of Fig. 7 presents the angular variations of mass transfer coefficients for the moisture diffusivity and blockage ratio ranges of $D=1\times10^{-5}-1\times10^{-8}$ m^2/s and $\beta=0.200-0.800$, respectively. The mass transfer coefficient curves are similar to those of Nusselt number (Fig. 6(*c*)) due to the dependent character of h_m on h_θ (Eq. (6*i*)). Moreover, since h_θ values, thus Nu_θ, are evaluated to grow with β (Fig. 6(*c*)), the identical impact can also be visualized on the β driven h_m characteristics. On the other hand, Fig. 7 clarifies that mass transfer coefficients significantly decrease in lower moisture diffusivity cases, which can be regarded as an indicator for considerably augmented overall drying times. Besides, the overall mean $\bar{h}_m$, front face mean $\bar{h}_{m-ff}$, and back face mean $\bar{h}_{m-bf}$ mass transfer coefficients are given in Table 2 for the investigated moisture diffusivity and blockage ratio scenarios. Showing harmony with Fig. 7, the tabulated data indicate that (i) $\bar{h}_{m-ff}$ are higher than $\bar{h}_m$ and $\bar{h}_{m-bf}$, which in return points out that the

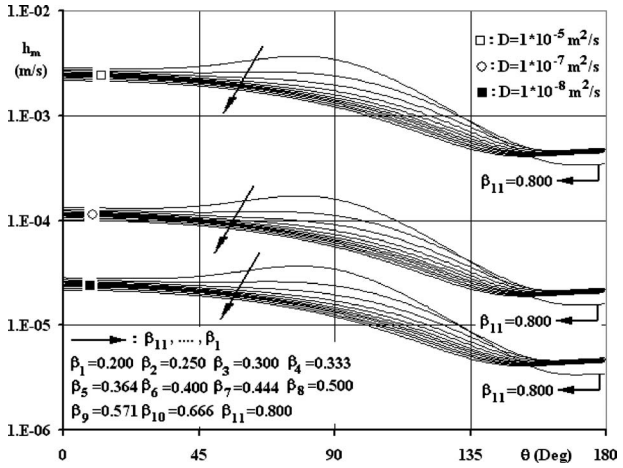

Fig. 7 Variation of mass transfer coefficients for the moisture diffusivity and blockage ratio ranges of $D=1\times10^{-5}-1\times10^{-8}$ m^2/s and $\beta=0.200-0.800$

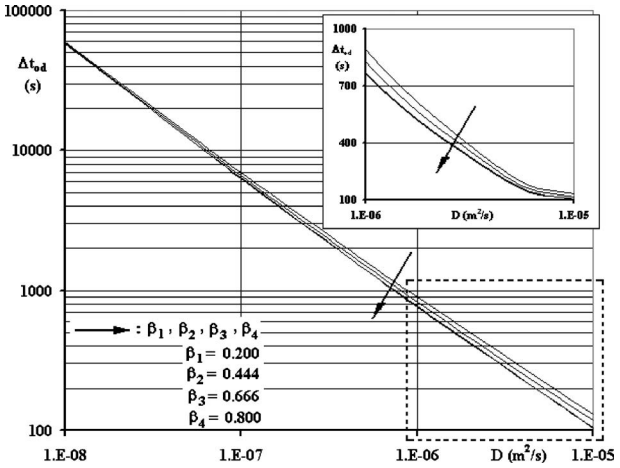

Fig. 8 Variation of overall drying times for the moisture diffusivity and blockage ratio ranges of $D=1\times10^{-5}-1\times10^{-8}$ m^2/s and $\beta=0.200-0.800$

potential of the moisture transfer in the front face of the cylinder is superior to that of the back face; (ii) the increasing role of β on mass transfer rates can be sensed both at the front ($\bar{h}_{m-ff}$) and back ($\bar{h}_{m-bf}$) faces; (iii) being independent of β, lower D decreases the mass transfer coefficients in every angular position of the cylinder surface. Table 2 additionally puts forward specific information regarding the influence of β on h_m. Computations show that as the $\bar{h}_{m-ff}/\bar{h}_m$ and $\bar{h}_{m-bf}/\bar{h}_m$ ratios attain the values of ~1.50 and ~0.50 for $\beta=0.200$, they become ~1.43 and ~0.57 with the rise of β to 0.800, where these proportions are also determined to be independent of D. These ratios identify that, although higher β augments the h_m on the overall cylinder surface (Fig. 7 and Table 2), the growing rate of $\bar{h}_{m-bf}$ is dominant to that of $\bar{h}_{m-ff}$ resulting in the rise of $\bar{h}_{m-bf}/\bar{h}_m$ and drop of $\bar{h}_{m-ff}/\bar{h}_m$ with higher blockage.

Figure 8 presents the overall drying times (Δt_{od}) for the moisture diffusivity and blockage ratio ranges of $D=1\times10^{-5}-1\times10^{-8}$ m^2/s and $\beta=0.200-0.800$. The log-log plot expresses the decrease style of Δt_{od} with both higher diffusivity and higher blockage ratio. As lower Δt_{od} at higher D is an expected outcome, the impact of β on Δt_{od} can be outlined by the direct relation of mass (h_m) and heat transfer (h_θ) coefficients through Eq. (6*i*). As extensively discussed in Sec. 3.1, heat transfer rates grow at higher blockage cases, which in return augments the mass transfer coefficients as presented in Fig. 7. Specifically denoting, computations resulted in the Δt_{od} of 59950→57402 s ($\beta=0.200\rightarrow0.800$) for $D_1=1\times10^{-8}$ m^2/s, 6915.4→6329.6 s for $D_2=1\times10^{-7}$ m^2/s, 894.48→766.12 s for $D_3=1\times10^{-6}$ m^2/s, and 131.41→103.55 s for $D_4=1\times10^{-5}$ m^2/s. These values point out the $\Delta t_{od-\beta=0.200}/\Delta t_{od-\beta=0.800}$ ratios of 1.044, 1.093, 1.168, and 1.269 for D_1, D_2, D_3, and D_4, respectively. The increasing nature of these ratios with higher D clearly puts forward that the impact of β on mass transfer becomes more effective at high D cases. On the other hand, the ratio of the overall drying times, among different diffusivity levels, clarifies the role of D on Δt_{od}. As the $\Delta t_{od-D_1}/\Delta t_{od-D_2}$ ratio is 8.67→9.07 ($\beta=0.200\rightarrow0.800$), the corresponding values for D_2 and D_3, and D_3 and D_4 are 7.73→8.26 and 6.81→7.40, respectively. These ratios indicate that extensive overall drying times can arise for a subject product with sufficiently low moisture diffusivity. This determination is quite important for drying applications, due to the fact that moisture diffusivity property can be as low as $D=1\times10^{-15}$ m^2/s [34].

3.2.2 In-Time Moisture Variations. The in-time variation of cylinder average (ϕ_a) and cylinder center (ϕ_c) dimensionless moisture contents are given in Figs. 9(*a*) and 9(*b*), respectively. As $\phi=1.00$ stands for the initial (t=0 s) moisture content ($M_{cyl}=3$ kg/kg), $\phi=0.00$ indicates the completely dry product and corresponding time is the overall drying time (Δt_{od}). Figure 9

Table 2 Variation of overall, front face, and back face average mass transfer coefficients for the moisture diffusivity and blockage ratio ranges of $D=1\times10^{-5}-1\times10^{-8}$ m^2/s and $\beta=0.200-0.800$

		$\beta=0.200$	$\beta=0.444$	$\beta=0.666$	$\beta=0.800$
$D=1\times10^{-5}$ m^2/s	$\bar{h}_m$ (m/s)	1.23×10^{-03}	1.48×10^{-03}	1.85×10^{-03}	2.18×10^{-03}
	$\bar{h}_{m\text{-}ff}$ (m/s)	1.84×10^{-03}	2.17×10^{-03}	2.61×10^{-03}	3.12×10^{-03}
	$\bar{h}_{m\text{-}bf}$ (m/s)	6.18×10^{-04}	7.94×10^{-04}	1.09×10^{-03}	1.25×10^{-03}
$D=1\times10^{-7}$ m^2/s	$\bar{h}_m$ (m/s)	5.69×10^{-05}	6.87×10^{-05}	8.60×10^{-05}	1.01×10^{-04}
	$\bar{h}_{m\text{-}ff}$ (m/s)	8.52×10^{-05}	1.01×10^{-04}	1.21×10^{-04}	1.45×10^{-04}
	$\bar{h}_{m\text{-}bf}$ (m/s)	2.87×10^{-05}	3.68×10^{-05}	5.07×10^{-05}	5.80×10^{-05}
$D=1\times10^{-8}$ m^2/s	$\bar{h}_m$ (m/s)	1.23×10^{-05}	1.48×10^{-05}	1.85×10^{-05}	2.18×10^{-05}
	$\bar{h}_{m\text{-}ff}$ (m/s)	1.84×10^{-05}	2.17×10^{-05}	2.61×10^{-05}	3.12×10^{-05}
	$\bar{h}_{m\text{-}bf}$ (m/s)	6.18×10^{-06}	7.94×10^{-06}	1.09×10^{-05}	1.25×10^{-05}

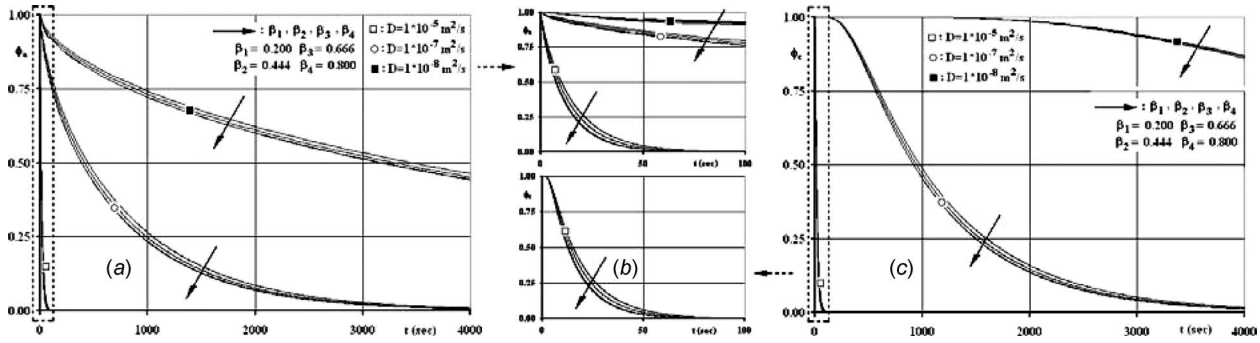

Fig. 9 In time variation of (*a*) cylinder average and (*b*) cylinder center dimensionless moisture content for the moisture diffusivity and blockage ratio ranges of $D=1\times10^{-5}-1\times10^{-8}$ m²/s and $\beta=0.200-0.800$

puts forward that as the ϕ_a and ϕ_c variations of the highest moisture diffusivity case ($D=1\times10^{-5}$ m²/s) are similar, apparent shifts arise among the average and center moisture curves for lower diffusivity products. The ϕ_c/ϕ_a ratios are presented in Table 3 for three diffusivity and two blockage ratio cases at five instants of the overall drying times. Tabulated values mainly indicate the following five issues: (i) Being independent of moisture diffusivity and blockage ratio levels, the gap among the center and average moisture content values is maximum in the early stages of the drying process; (ii) for products with lower diffusivity, the gap is superior to those of the higher diffusivity products; (iii) in higher blockage cases, due to higher mass transfer coefficients, the gap is above those of the lower blockage cases; (iv) in the last 5% of the drying period, center and average moisture content values converge by a ≤1.6% gap, indicating a homogeneous moisture distribution inside the product; (v) during drying, by investigating the weight change of the product, or the amount of lost moisture, the current total moisture content and the average moisture level can be calculated. However the present findings put forward that due to not only the moisture diffusivity of the product but also the blockage ratio of the flow domain, the center moisture value can be significantly above the average moisture level. Thus, the drying period must be decided by considering both the average and center moisture levels. The present computations further point out that 97.75–98.50% of the excess moisture content (M_{cyl}-M_a) leaves the product in the first half of the overall drying time ($\Delta t_{od}/2$). Since operation cost is of high importance in industrial drying applications, this determination enlightens the necessity of accurate estimation of drying period for the desired drying level.

The local dimensionless moisture content variations of three surface points ($S_1-\theta=0$ deg, $S_2-\theta=180$ deg, and $S_3-\theta=90$ deg), as given in Fig. 1(*b*), are plotted in Fig. 10 for the blockage ratio and moisture diffusivity ranges of $\beta=0.200-0.800$ and $D=1\times10^{-5}-1\times10^{-8}$ m²/s, respectively. The figure puts forward that, being independent of β, at the highest moisture diffusivity scenario of $D=1\times10^{-5}$ m²/s, sharp decreases in moisture occur on the cylinder surface with the start of drying ($t\leq100$ s), where the dimensionless moisture values decay down almost to $\phi=0.00$. This outcome can be explained by the simultaneous role of the high mass transfer coefficients and the high moisture diffusion inside the cylinder due to high D. Figure 10 further indicates for $D=1\times10^{-8}$ m²/s, the ϕ difference among S_1 and S_3 locations becomes apparent and wider at lower β. The source of the difference can be clarified by the mass transfer coefficients given in Fig. 7. Figure 7 shows that although the queue of $h_{m-S_1}>h_{m-S_3}$ remains fixed, the gaps among the h_m values become broader at lower β. It can be seen from Fig. 10 that, if each moisture diffusivity case is considered individually, at higher blockage ratios considerably lower moisture exist at S_1 and S_3, but the contrary is true for S_2, which can as well be attributed to the variation of mass transfer coefficients on the cylinder surface (Fig. 7). Computations additionally clarified that, for the complete moisture diffusivity range investigated, as the state of the surface moisture layout, in the highest blockage case of $\beta=0.800$, comes out to be sequenced as $\phi_{S_2}>\phi_{S_1}>\phi_{S_3}$, in the flows with $\beta\leq0.666$ the order of the moisture contents at S_1 and S_3 replaces resulting in $\phi_{S_2}>\phi_{S_3}>\phi_{S_1}$. This finding puts forward the fact that surface moisture levels are characterized significantly by h_m and secondarily by D. These evaluations are extremely important from the point that blockage effect can be adapted to drying applications in which forced-drying is required to be directed to certain angular locations of CC products.

3.2.3 Isomoisture Contour Layouts. Isocontours, at the 10% overall drying times are plotted in Figs. 11(*a*)–11(*c*) for the moisture diffusivities of $D=1\times10^{-5}$ m²/s, $D=1\times10^{-6}$ m²/s, and $D=1\times10^{-7}$ m²/s, respectively. It can be seen from the figure that the front face moisture levels are lower than those of the back face, being independent of moisture diffusivity and blockage ratio. These determinations completely match the in-time moisture variations (Fig. 10) of the surface points S_1 and S_2. Through the numerical analyses the gap among ϕ_{max} and the moisture contents

Table 3 Variation of center to average dimensionless moisture content ratios at five instants of the overall drying times for the moisture diffusivity and blockage ratio ranges of $D=1\times10^{-5}-1\times10^{-8}$ m²/s and $\beta=0.200-0.800$

	ϕ_c/ϕ_a					
	$D=1\times10^{-5}$ m²/s		$D=1\times10^{-7}$ m²/s		$D=1\times10^{-8}$ m²/s	
	$\beta=0.200$	$\beta=0.800$	$\beta=0.200$	$\beta=0.800$	$\beta=0.200$	$\beta=0.800$
5% Δt_{od}	1.337	1.442	1.609	1.674	1.715	1.759
25% Δt_{od}	1.284	1.380	1.539	1.589	1.629	1.664
50% Δt_{od}	1.119	1.160	1.277	1.301	1.334	1.350
75% Δt_{od}	1.024	1.032	1.056	1.060	1.066	1.070
95% Δt_{od}	1.006	1.007	1.012	1.014	1.015	1.016

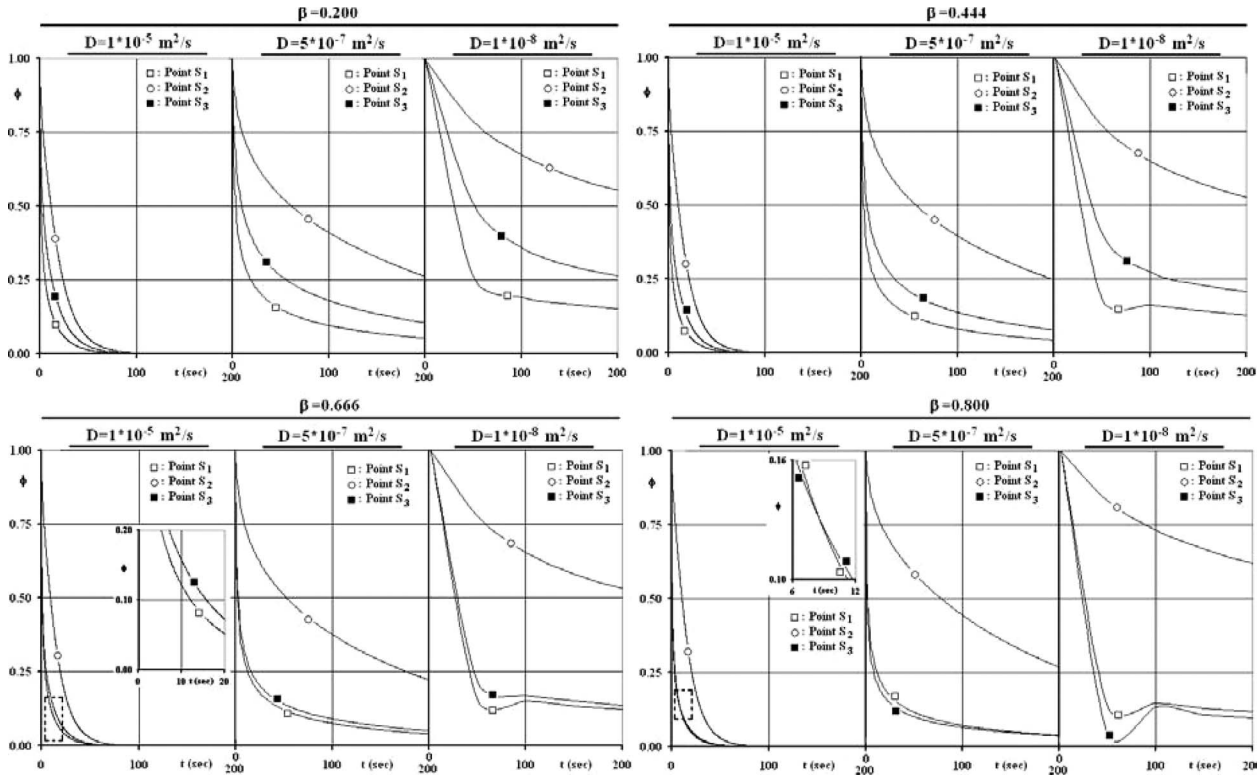

Fig. 10 Drying characteristics at the cylinder surface locations of S_1, S_2, and S_3 for the moisture diffusivity and blockage ratio ranges of $D=1\times10^{-5}-1\times10^{-8}$ m^2/s and $\beta=0.200-0.800$

of S_1 ($\theta=0$ deg) and S_2 ($\theta=180$ deg) (Fig. 1(*b*)) are also identified. As ϕ_{max} exceeds ϕ_{S_1} and ϕ_{S_2} by $0.476\rightarrow0.521$ and $0.146\rightarrow0.122$ ($\beta=0.200\rightarrow0.800$) at $D=1\times10^{-5}$ m^2/s, these differences grow up to $0.650\rightarrow0.676$ and $0.476\rightarrow0.457$ at $D=1\times10^{-7}$ m^2/s. These figures, besides being consistent with the ϕ_c/ϕ_a ratios of Table 3, not only notify the decrease of $\phi_{max}-\phi_{S_2}$ and increase of $\phi_{max}-\phi_{S_1}$ with higher blockage ratios, but also identify the rise of the maximum to surface moisture level gap in cases with lower moisture diffusivities. Figure 11 additionally indicates that as the ϕ_{max} locations are separated from cylinder center in the moisture diffusivity scenario of $D=1\times10^{-5}$ m^2/s, those of $D=1\times10^{-7}$ m^2/s are located in the vicinity of the cylinder center in the complete blockage range considered ($\beta=0.200-0.800$). This evaluation puts forward that in drying applications with high moisture diffusivities ($D=1\times10^{-5}$ m^2/s) surface mass transfer coefficients (h_m) are quite determinative on the front and back face moisture levels. However, in cases with lower diffusivity ($D\leq1\times10^{-7}$ m^2/s) moisture levels on the front and back faces become closer and the ϕ_{max} location shifts toward the cylinder center. The mechanism of this evaluation can further be identified through the converging nature of above $\phi_{max}-\phi_{S_1}$ and $\phi_{max}-\phi_{S_2}$ differences in lower moisture diffusivities. It can further be extracted from the figure that the $\phi_{max(\beta=0.200)}$ and $\phi_{max(\beta=0.800)}$ values diverge at high D cases; such that as the $\phi_{max(\beta=0.200)}$-$\phi_{max(\beta=0.800)}$ difference for $D=1\times10^{-7}$ m^2/s is 0.017, it grows to 0.025 and 0.026 at $D=1\times10^{-6}$ m^2/s and $D=1\times10^{-5}$ m^2/s, respectively. These evaluations put forward the fact that the role of β, and the so occurring h_m distribution, on ϕ_{max} and ϕ_{max} location becomes ineffective at low moisture diffusivities. The discussions presented in Fig. 11 are essential in generating a theoretical approach based scientific relation among the surface and maximum moisture levels.

3.2.4 Verification Analysis. The scientific standard and precision of the new ADI based software is verified by computationally handling the experimental results of Queiroz and Nebra [21] for the drying process of bananas ($D=4.59\times10^{-10}$ m^2/s). Queiroz and Nebra [21] conducted their drying experiments in a laboratory convective chamber dryer. The equipment was supported with a data acquisition device that allowed controlling the air drying conditions, such as temperature and relative humidity, and automatically recorded these parameters and the weight loss data during the entire process. Similar to the present study, the fruit with cylindrical cross section was placed in the perforated tray of the chamber dryer in the direction of air flow. Figure 12 indicates that the outputs of the present model, computed with the experimental conditions of Ref. [21] ($U_\infty=0.33$ m/s, $T_\infty=39.9°C$, $h_m=1.66\times10^{-7}$ m/s, and $M_i=3.43$ kg/kg), and the experimental findings of Ref. [21] coincide well with an acceptable average deviation of 6.4%.

4 Conclusions

The present paper has introduced and discussed the results of a comprehensive numerical investigation on fluid flow and heat-mass transfer characteristics of a circular cylinder, subjected to confined flow. The key concluding remarks of the present study can be summarized as follows:

1. Blockage shifts separation and maximum C_f locations downstream to the positions of $\theta_s=54.10$ deg and 37.30 deg and $\theta_{C_f-max}=51.5$ deg and 85.4 deg for $\beta=0.200$ and 0.800.
2. The lengths of the recirculation zones are computed as to decrease with β, indicating that blockage negatively affects the influential domain and strength of the downstream vortex system.
3. On the overall cylinder surface, blockage is determined to cause thinner hydrodynamic and thermal boundary layers, which in return also rises the frictional and thermal activity.
4. The late hydrodynamic response of the upstream flow do-

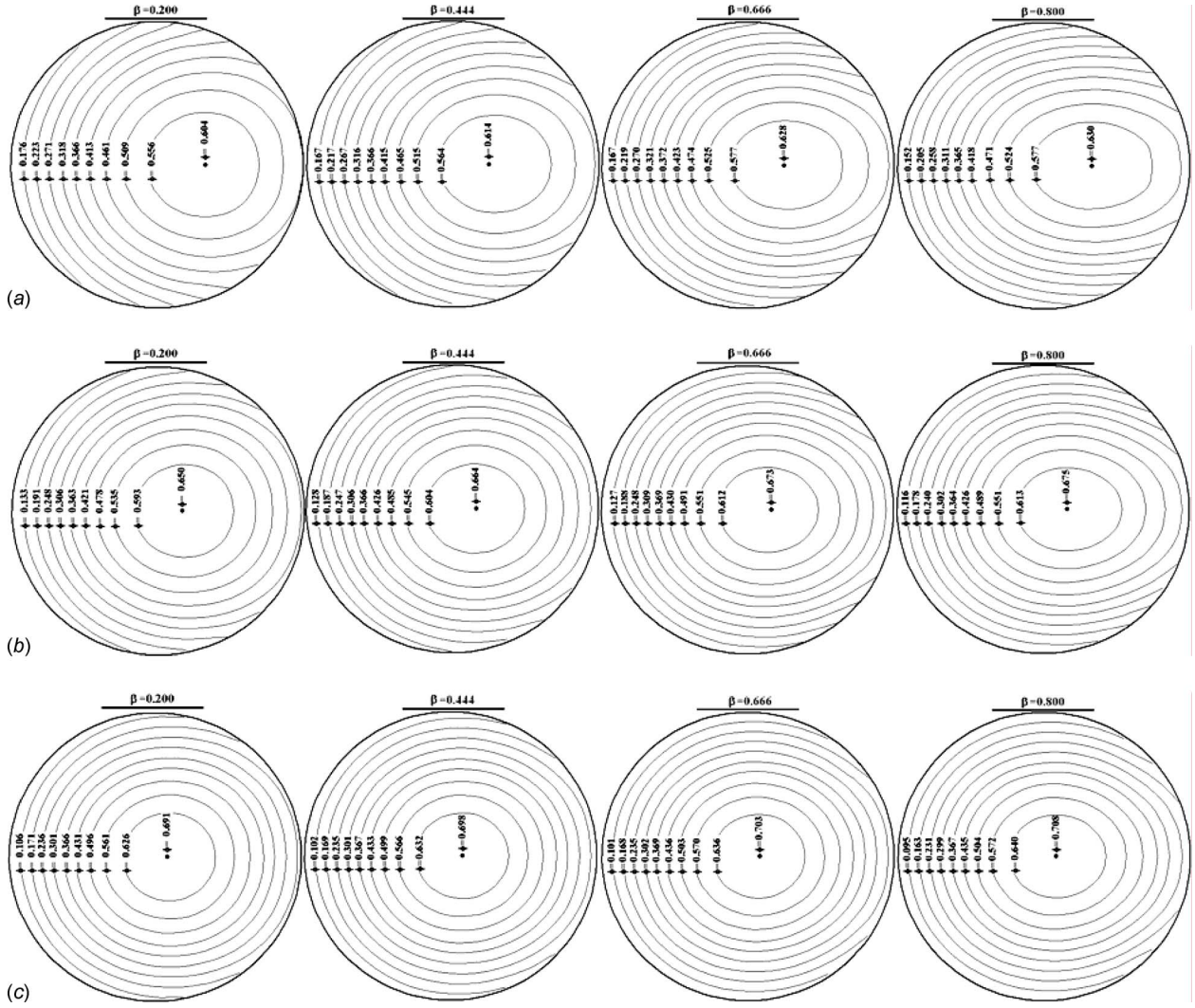

Fig. 11 Isomoisture contours at the 10% drying times of the cases with (*a*) $D=1\times10^{-5}$ m^2/s, (*b*) $D=1\times10^{-6}$ m^2/s, and (*c*) $D=1\times10^{-7}$ m^2/s for the blockage ratios of $\beta=0.200$, 0.444, 0.666, and 0.800

main at higher β scenarios decelerates the flowing air more rapidly to zero toward the stagnation point and results in augmented momentum velocity in the neighborhood of the cylinder and elevated pressure coefficient values.

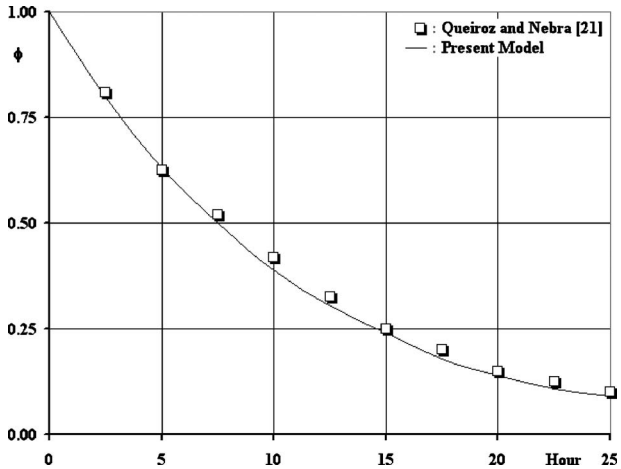

Fig. 12 Comparison of the present model with the experimental outputs of Queiroz and Nebra [21]

5. The Nusselt numbers are determined to be most promoted by blockage at the throat, which in return indicates that the heat transfer mechanism is more influenced by boundary layer thinning than the upstream momentum activity.
6. The higher stagnation point Nusselt number range of $Nu=8.53\rightarrow6.49$ ($\beta=0.800\rightarrow0.200$) than those of the back face values ($Nu=1.03\rightarrow1.31$) at $\theta=180$ deg put forward the superior potential of the stagnation point momentum activity to the downstream vortex system from the point of heat transfer enhancing capability.
7. Besides demonstrating the upstream stand of minimum C_p locations with respect to θ_s, the present computations as well indicated that the gap among θ_s and θ_{C_p-min} becomes narrower at stronger blockage, where the interpreting values are θ_s-$\theta_{C_p-min}=37.6$ deg and 32.8 deg for $\beta=0.200$ and 0.800.
8. The ratios of overall drying times ($\Delta t_{od-\beta=0.200}/\Delta t_{od-\beta=0.800}$), among the limiting blockage scenarios of $\beta=0.200-0.800$, are computed as 1.044–1.269 for $D=1\times10^{-8}$ m^2/s and 1×10^{-5} m^2/s, respectively, identifying the rising role β on mass transfer with higher D.
9. Higher β augments the h_m on the overall cylinder surface;

however, the growing rate of $\bar{h}_{m-bf}$ is dominant to that of $\bar{h}_{m-ff}$.

Nomenclature

C_f = friction coefficient
C_p = constant pressure specific heat (J/kg K), pressure coefficient
d = diameter (m)
D = moisture diffusivity (m^2/s)
h = convective heat transfer coefficient (W/m^2 K)
h_m = mass transfer coefficient (m/s)
H = duct height (m)
k = conductive heat transfer coefficient (W/m K)
Le = Lewis number
L_r = recirculation length (m)
M = moisture content (kg/kg)
n = normal direction
Nu = Nusselt number
P = static pressure (Pa)
r = radical direction
Re_{ch} = channel Reynolds number
Re_d = cylinder Reynolds number
t = time (s)
T = temperature (K)
u = velocity in x-direction (m/s)
U_∞ = average velocity of air at the inlet (m/s)
v = velocity in y-direction (m/s)
w = width (mm)
x = coordinate in x-direction (m)
y = coordinate in y-direction (m)

Greek Symbols

α = thermal diffusivity (m^2/s)
β = blockage ratio
Δ = difference
ϕ = dimensionless moisture
λ = under-relaxation parameter
μ = dynamic viscosity (Pa s)
θ = angular position (deg)
ρ = density (kg/m^3)
τ_s = shear stress (Pa)
ζ = dimensionless temperature

Subscripts

a = air, average
bf = back face
c = center
cyl = cylinder
ds = downstream
ff = front-face
i = initial
od = overall drying
max = maximum
n = normal to the cylinder surface
θ = angular
rev = reverse
s = separation, cylinder surface
th = throat
us = upstream
∞ = inlet air

Superscript

_ = average

References

[1] Bhattacharyya, S., Dhinakaran, S., and Khalili, A., 2006, "Fluid Motion Around and Through a Porous Cylinder," Chem. Eng. Sci., **61**, pp. 4451–4461.
[2] Job, N., Sabatier, F., Pirard, J. P., Crine, M., and Leonard, A., 2006, "Towards the Production of Carbon Xerogel Monoliths by Optimizing Convective Drying Conditions," Carbon, **44**, pp. 2534–2542.
[3] Akpinar, E. K., and Dincer, I., 2005, "Moisture Transfer Models for Slabs Drying," Int. Commun. Heat Mass Transfer, **32**, pp. 80–93.
[4] Griffith, M. D., Thompson, M. C., Leweke, T., Hourigan, K., and Anderson, W. P., 2007, "Wake Behaviour and Instability of Flow Through a Partially Blocked Channel," J. Fluid Mech., **582**, pp. 319–340.
[5] Chakraborty, J., Verma, N., and Chhabra, R. P., 2004, "Wall Effects in Flow Past a Circular Cylinder in a Plane Channel: A Numerical Study," Chem. Eng. Process., **43**, pp. 1529–1537.
[6] Sahin, M., and Owens, R. G., 2004, "A Numerical Investigations of Wall Effects Up to High Blockage Ratios on Two-Dimensional Flow Past a Confined Circular Cylinder," Phys. Fluids, **16**, pp. 1305–1320.
[7] Rehimi, F., Aloui, F., Nasrallah, S. B., Doubliez, L., and Legrand, J., 2008, "Experimental Investigation of a Confined Flow Downstream of a Circular Cylinder Centred Between Two Parallel Walls," J. Fluids Struct., **24**, pp. 855–882.
[8] Sen, S., Mittal, S., and Biswas, G., 2009, "Steady Separated Flow Past a Circular Cylinder at Low Reynolds Numbers," J. Fluid Mech., **620**, pp. 89–119.
[9] Breuer, M., Bernsdorf, J., Zeiser, T., and Durst, F., 2000, "Accurate Computations of the Laminar Flow Past a Square Cylinder Based on Two Different Methods: Lattice-Boltzmann and Finite-Volume," Int. J. Heat Fluid Flow, **21**, pp. 186–196.
[10] Camarri, S., and Giannetti, F., 2007, "On the Inversion of the von Karman Street in the Wake of a Confined Square Cylinder," J. Fluid Mech., **574**, pp. 169–178.
[11] Chang, B. H., and Mills, A. F., 2004, "Effect of Aspect Ratio on Forced Convection Heat Transfer From Cylinders," Int. J. Heat Mass Transfer, **47**, pp. 1289–1296.
[12] Khan, W. A., Culham, J. R., and Yovanovich, M. M., 2005, "Fluid Flow Around and Heat Transfer From an Infinite Circular Cylinder," ASME J. Heat Transfer, **127**, pp. 785–790.
[13] Khan, W. A., Culham, J. R., and Yovanovich, M. M., 2006, "Analytical Study of Heat Transfer From Circular Cylinder in Liquid Metals," Heat Mass Transfer, **42**, pp. 1017–1023.
[14] Bharti, R. P., Chhabra, R. P., and Eswaran, V., 2007, "Effect of Blockage on Heat Transfer From a Cylinder to Power Law Liquids," Chem. Eng. Sci., **62**, pp. 4729–4741.
[15] Montelpare, S., and Ricci, R., 2004, "An Experimental Method for Evaluating the Heat Transfer Coefficient of Liquid-Cooled Short Pin Fins Using Infrared Thermography," Exp. Therm. Fluid Sci., **28**, pp. 815–824.
[16] Sparrow, E. M., Abraham, J. P., and Tong, J. C. K., 2004, "Archival Correlations for Average Heat Transfer Coefficients for Non-Circular and Circular Cylinders and for Spheres in Cross-Flow," Int. J. Heat Mass Transfer, **47**, pp. 5285–5296.
[17] Buyruk, E., Johnson, M. W., and Owen, I., 1998, "Numerical and Experimental Study of Flow and Heat Transfer around a Tube in Cross-Flow at Low Reynolds Number," Int. J. Heat Fluid Flow, **19**, pp. 223–232.
[18] Khan, W. A., Culham, J. R., and Yovanovich, M. M., 2004, "Fluid Flow and Heat Transfer from a Cylinder between Parallel Planes," J. Thermophys. Heat Transfer, **18**, pp. 395–403.
[19] Sharma, A., and Eswaran, V., 2004, "Effect of Channel Confinement on the Two-Dimensional Laminar Flow and Heat Transfer Across a Square Cylinder," Numer. Heat Transfer, Part A, **47**, pp. 79–107.
[20] Dhiman, A. K., Chhabra, R. P., and Eswaran, V., 2005, "Flow and Heat Transfer across a Confined Square Cylinder in the Steady Flow Regime: Effect of Peclet Number," Int. J. Heat Mass Transfer, **48**, pp. 4598–4614.
[21] Queiroz, M. R., and Nebra, S. A., 2001, "Theoretical and Experimental Analysis of the Drying Kinetics of Bananas," J. Food. Eng., **47**, pp. 127–132.
[22] Dincer, I., Hussain, M. M., Sahin, A. Z., and Yilbas, B. S., 2002, "Development of a New Moisture Transfer (Bi–Re) Correlation for Food Drying Applications," Int. J. Heat Mass Transfer, **45**, pp. 1749–1755.
[23] Akpinar, E. K., and Dincer, I., 2005, "Application of Moisture Transfer Models to Solids Drying," Proc. Inst. Mech. Eng., Part A, **219**, pp. 235–244.
[24] Kaya, A., Aydin, O., and Dincer, I., 2007, "Numerical Modeling of Forced Convection Drying of Cylindrical Moist Objects," Numer. Heat Transfer, Part A, **51**, pp. 843–854.
[25] Sahin, A. Z., and Dincer, I., 2002, "Graphical Determination of Drying Process and Moisture Transfer Parameters for Solids Drying," Int. J. Heat Mass Transfer, **45**, pp. 3267–3273.
[26] Feng, H., Tang, J., and Dixon-Warren, J., 2000, "Determination of Moisture Diffusivity of Red Delicious Apple Tissues by Thermogravimetric Analysis," Drying Technol., **18**, pp. 1183–1199.
[27] Hussain, M. M., and Dincer, I., 2003, "Two-Dimensional Heat and Moisture Transfer Analysis of a Cylindrical Moist Object Subjected to Drying: A Finite-Difference Approach," Int. J. Heat Mass Transfer, **46**, pp. 4033–4039.
[28] Sahin, A. Z., Dincer, I., Yilbas, B. S., and Hussain, M. M., 2002, "Determination of Drying Times for Regular Multi-Dimensional Objects," Int. J. Heat Mass Transfer, **45**, pp. 1757–1766.
[29] Kondjoyan, A., 2006, "A Review on Surface Heat and Mass Transfer Coefficients During Air Chilling and Storage of Food Products," Int. J. Refrig., **29**, pp. 863–875.
[30] Dincer, I., and Hussain, M. M., 2002, "Development of a New Bi–Di Correlation for Solids Drying," Int. J. Heat Mass Transfer, **45**, pp. 3065–3069.
[31] Araszkiewicz, M., Koziol, A., Lupinska, A., and Lupinski, M., 2007, "Microwave Drying of Various Shape Particles Suspended in an Air Stream," Transp.

Porous Media, **66**, pp. 173–186.
[32] McMinn, W. A. M., and Magee, T. R. A., 1996, "Air Drying Kinetics of Potato Cylinders," Drying Technol., **14**, pp. 2025–2040.
[33] Gögus, F., and Maskan, M., 1999, "Water Adsorption and Drying Characteristics of Okra (Hibiscus Esculenuts L.)," Drying Technol., **17**, pp. 883–894.
[34] Panagiotou, N. M., Krokida, M. K., Maroulis, Z. B., and Saravacos, G. D., 2004, "Moisture Diffusivity: Literature Data Compilation for Foodstuffs," Int. J. Food Prop., **7**, pp. 273–299.
[35] Incropera, F. P., and De Witt, D. P., 1990, *Fundamentals of Heat and Mass Transfer*, Wiley, New York.
[36] 2005, ANSYS-CFX User Manual.
[37] Kaya, A., Aydin, O., and Dincer, I., 2006, "Numerical Modeling of Heat and Mass Transfer During Forced Convection Drying of Rectangular Moist Objects," Int. J. Heat Mass Transfer, **49**, pp. 3094–3103.
[38] Krokida, M. K., Foundoukidis, E., and Maroulis, Z., 2004, "Drying Constant: Literature Data Compilation for Foodstuffs," J. Food. Eng., **61**, pp. 321–330.
[39] Simal, S., Rossell, C., Berna, A., and Mulet, A., 1998, "Drying of Shrinking Cylinder-Shaped Bodies," J. Food. Eng., **37**, pp. 423–435.
[40] Kawaguti, M., and Jain, P., 1966, "Numerical Study of a Viscous Fluid Flow Past a Circular Cylinder," J. Phys. Soc. Jpn., **61**, pp. 1998–2055.
[41] Biswas, G., and Sarkar, S., 2009, "Effect of Thermal Buoyancy on Vortex Shedding Past a Circular Cylinder in Cross-Flow at Low Reynolds Numbers," Int. J. Heat Mass Transfer, **52**, pp. 1897–1912.
[42] Takami, H., and Keller, H. B., 1969, "Steady Two-Dimensional Viscous Flow of an Incompressible Fluid Past a Circular Cylinder," Phys. Fluids, **12**, pp. II-51–II-56.
[43] Dennis, S. C. R., and Chang, G.-Z., 1970, "Numerical Solutions for Steady Flow Past a Circular Cylinder at Reynolds Numbers up to 100," J. Fluid Mech., **42**, pp. 471–489.
[44] Zukauskas, A., and Ziugzda, J., 1985, *Heat Transfer of a Cylinder in Crossflow*, Hemisphere, New York.
[45] Schönauer, W., 1964, "Ein Differenzenverfahren zur Lösung der Grenzschichtgleichung für Stationäre, Laminare, Inkompressible Strömung," Ing.-Arch., **33**, pp. 173.
[46] Jafroudi, H., and Yang, H. T., 1986, "Steady Laminar Forced Convection From a Circular Cylinder," J. Comput. Phys., **65**, pp. 46–56.
[47] Apelt, C. J., and Ledwich, M. A., 1979, "Heat Transfer in Transient and Unsteady Flows Past a Circular Cylinder in the Range $1 < Re < 40$," J. Fluid Mech., **95**, pp. 761–777.
[48] Ozalp, A. A., and Umur, H., 2003, "An Experimental Investigation of the Combined Effects of Surface Curvature and Streamwise Pressure Gradients Both in Laminar and Turbulent Flows," Heat Mass Transfer, **39**, pp. 869–876.
[49] Umur, H., and Ozalp, A. A., 2006, "Fluid Flow and Heat Transfer in Transitional Boundary Layers: Effects of Surface Curvature and Free Stream Velocity," Heat Mass Transfer, **43**, pp. 7–15.
[50] Ozalp, A. A., 2009, "Entropy Analysis of Laminar Forced Convection in a Pipe With Wall Roughness," Int. J. Exergy, **6**, pp. 249–275.
[51] Ozalp, A. A., 2008, "Roughness Induced Forced Convective Laminar-Transitional Micropipe Flow: Energy and Exergy Analysis," Heat Mass Transfer, **45**, pp. 31–46.
[52] Obot, N. T., 2002, "Toward a Better Understanding of Friction and Heat/Mass Transfer in Microchannels—A Literature Review," Microscale Thermophys. Eng., **6**, pp. 155–173.
[53] Turner, A. B., Hubbe-Walker, S. E., and Bayley, F. J., 2000, "Fluid Flow and Heat Transfer Over Straight and Curved Rough Surfaces," Int. J. Heat Mass Transfer, **43**, pp. 251–262.